Journal of Chromatography A, 1217 (2010) 8103–8120

Contents lists available at ScienceDirect

Journal of Chromatography A

journal homepage: www.elsevier.com/locate/chroma

A parallel pore and surface diffusion model for predicting the adsorption and elution profiles of lispro insulin and two impurities in gradient-elution reversed phase chromatography

Pei-Lun Chung, Jennifer Galvez Bugayong[1], Chim Yong Chin[2], Nien-Hwa Linda Wang*

School of Chemical Engineering, Purdue University, 480 Stadium Mall Drive, West Lafayette, IN 47907-2100, USA

ARTICLE INFO

Article history:
Received 6 August 2010
Accepted 28 September 2010
Available online 7 October 2010

Keywords:
Insulin
Reversed phase chromatography
Isotherm parameter estimation
Stepwise elution
Linear gradient elution
Parallel pore and surface diffusion

ABSTRACT

Lispro insulin (LPI), a widely used insulin analog, is produced on tons per year scale. Linear gradient reversed phase chromatography (RPC) is used in the production to separate LPI from two impurities, which differ from LPI by a single amino acid residue. A chromatography model for the ternary separation in this RPC process is unavailable from the literature. In this study, a parallel pore and surface diffusion model is developed and verified for LPI and the two impurities. The LPI can be recovered with high yield (≥95%) and high purity (>99.5%). A new method, which requires a small amount of materials and an order of magnitude fewer experiments, has been developed to estimate the solvent-modulated isotherm parameters. A modified reversed phase modulator model is developed to correlate the adsorption isotherms of LPI and impurities. A strategy has been developed for estimating the intrinsic pore diffusivity and surface diffusivity. Since the adsorption affinities decrease by more than three orders of magnitude as organic fraction (φ) increases from 0.19 to 0.40, the apparent diffusivities based on a pore diffusion model or a surface diffusion model can also vary by several orders of magnitude. For this reason, a pore diffusion model or a surface diffusion model with a constant apparent diffusivity cannot predict closely the chromatograms over the same range of organic fractions, concentrations, and loadings. The parallel pore and surface diffusion model with constant diffusivities can predict closely the frontal and elution profiles over a wide range of organic fractions (0.19–0.40), LPI concentrations (0.05–18 g/L), linear velocities (<10 cm/min), and loading volume (0.0004–13 CV). For large loading stepwise and linear gradient elution, the peaks of LPI and the impurities are strongly focused by self-sharpening and gradient focusing effects as a result of the steep decrease of adsorption affinity from the loading φ (0.19) to elution φ (≥0.27). When the ratio of diffusion rate to convection rate is greater than 10, spreading due to diffusion is largely compensated by the focusing effects. As a result, a pore diffusion model with a constant pore diffusivity can predict closely the elution profiles in stepwise and linear gradient elution. The experimental yield values (≥95%) can be predicted to within ±1% by the model.

1. Introduction

Insulin is the only recombinant therapeutic protein produced on tons per year scale [1]. Lispro insulin (LPI) is the first commercial insulin analog with a reversed sequence of proline and lysine on the B chain of insulin [2–6]. The reversed amino acid sequence reduces the tendency of self-association and makes LPI a fast-acting analog without affecting its therapeutic function. As a result, LPI has been widely used in the treatment of diabetes [7–9].

Reversed phase chromatography (RPC) is a key polishing step in insulin production [1]. The major goal of RPC is to remove two structurally similar impurities before size exclusion chromatography and crystallization [1,10]. Designing RPC for this separation is challenging for four reasons: (1) The RPC step must produce LPI with high purity (>99.5%). (2) LPI and the impurities have similar retention in RPC, because they have similar molecular structures. An early eluting impurity is a degraded product (DP), which differs from LPI by an amino acid residue. A late eluting impurity is A21-desamido LPI (A21), which has a missing amide group. Complete separation of LPI from the two impurities is challenging at high loading. (3) The adsorption affinities of LPI and impurities in RPC are highly sensitive to the solvent strength (or organic fraction) of the mobile phase. A small increase in organic fraction can cause several orders of magnitude decrease in adsorption affinity. (4) Multi-component competitive adsorption, desorption, and mass

* Corresponding author. Tel.: +1 765 494 4081; fax: +1 765 494 0805.
E-mail address: wangn@ecn.purdue.edu (N.-H.L. Wang).
[1] Current address: Praxair Inc., 175 East Park Drive, Tonawanda, NY 14150, USA.
[2] Current address: PureVision Technology, Inc. 511 McKinley Ave., Ft. Lupton, CO 80621, USA.

0021-9673/$ – see front matter © 2010 Elsevier B.V. All rights reserved.
doi:10.1016/j.chroma.2010.09.078

transfer behaviors of LPI and the impurities in RPC linear gradient elution are not well understood.

A major objective of this study is to build a chromatography model, which can predict the adsorption and elution of LPI and the two impurities over a wide range of organic fractions, and loading/elution conditions. A second objective is to use the model to understand how the key adsorption, mass transfer, and operating parameters affect the peak shape in frontal, stepwise, and linear gradient elution. The model can also be used in process designs to improve peak resolution and yield in a subsequent study.

Only a few chromatography models for insulin and related molecules in RPC have been reported. The two key elements in a chromatography model are (1) how to relate the concentrations in sorbent to those in solution, and (2) how to account for the mass transfer effects. The single component adsorption and elution of insulin has been modeled under isocratic conditions in RPC [11,12]. The adsorption and desorption were considered to be in equilibrium and the equilibrium concentrations in the two phases were correlated with the Toth isotherm. The isotherm parameters were estimated using frontal analysis. Either a pore diffusion model or a surface diffusion model closely predicted the isocratic elution profiles of insulin at a fixed organic solvent concentration (31 vol.% acetonitrile). However, it is unclear whether a pore diffusion or a surface diffusion model with constant diffusivity can predict elution profiles in frontal or linear gradient elution over a wide range of organic fractions.

A recent study reported a Langmuir kinetic model for insulin and desamido insulin in stepwise elution [13]. The linear and nonlinear Langmuir isotherm parameters were correlated with ethanol concentration in an exponential function (solvent-modulated). Axial dispersion was considered in this model, whereas the effects of film mass transfer and intraparticle diffusion were lumped with those of adsorption/desorption into a single Langmuir kinetic constant. The kinetic constant and the linear and nonlinear Langmuir parameters were estimated from stepwise elution profiles of small and large pulses, which were eluted at different ethanol concentrations (27 to 30%). The model closely predicted the profiles of insulin and desamido insulin eluted at 28%, but not at 26.6%. The authors attributed the errors to the extrapolation of isotherm parameters outside the experimental range. Other features of the literature models are summarized in Table 1. A multi-component model that predicts the elution profiles of insulin and the two impurities in linear gradient elution has not been reported. It is also unclear whether pore diffusion or surface diffusion should be considered in the model.

Ma et al. developed the most general rate model [14]. The solid phase concentration is related to the solution concentration by a solvent-modulated Langmuir kinetic rate expression. When the rate constants for adsorption and desorption are sufficiently large, the kinetic rate expression of each component reduces to a solvent-modulated competitive equilibrium Langmuir isotherm. The mass transfer mechanisms considered in this model include axial dispersion, film mass transfer, pore diffusion, and surface diffusion. This model has been tested for the adsorption of small organic molecules and ion exchange of small ions. We tested the model for LPI and the impurities in this study for two reasons: (1) at a low organic fraction, asymmetric breakthrough curves of LPI were observed and they could not be predicted by a pore diffusion model, and (2) the apparent pore diffusivity estimated from a pore diffusion model and the apparent surface diffusivity estimated from a surface diffusion model depend strongly on organic fraction and LPI concentration.

This study aims to answer the following research questions: (1) Under what conditions (temperature, solvent, and solvent strength) can adsorbed LPI be fully recovered? (2) Can the adsorption and desorption of LPI and impurities be described by a kinetic rate expression or an equilibrium isotherm? If the adsorption/desorption is in local equilibrium, what is the suitable isotherm model? (3) How can one estimate isotherm parameters over a wide range of organic fractions with a small number of experiments? (4) Which mass transfer mechanisms (pore diffusion, surface diffusion, or parallel pore and surface diffusion) need to be considered in the model in order to predict RPC frontal and linear gradient elution profiles of LPI and the impurities? How can one estimate the pore diffusivity and surface diffusivity independently?

In this study, the temperature and the loading and elution organic fractions which allow full recovery of LPI are first identified. Under such conditions, the adsorption and desorption of LPI and impurities can be described by an equilibrium isotherm. A modified reversed phase modulator isotherm is tested for the first time for LPI and the two impurities. The isotherm model requires four isotherm parameters for each component.

The most widely used method for estimating isotherm parameters is frontal analysis [11,12,15–17]. At a fixed organic fraction, more than 15 frontal experiments are needed to obtain a single adsorption isotherm for insulin [11]. To obtain accurate isotherms

Table 1
Comparison of this study with literature studies on chromatography models for insulin or analogs in reversed phase chromatography.

	Reference		This study
	[11,12]	[13]	
Chromatography model	Single component in isocratic elution	Two components in stepwise elution	Three components in linear gradient and stepwise elution
Types of isotherm model, # parameters for each component	Toth, 3 at each φ[a]	Solvent-modulated Langmuir kinetic, 3[b]	Modified solvent-modulated RPM, 4
Method for isotherm parameter estimation	Frontal analysis (FA)	Stepwise elution	Linear gradient elution and FA
Mass transfer model	Dispersion model, film diffusion lumped with either pore or surface diffusion model	Dispersion model, film and intraparticle diffusion lumped with kinetic constant	Parallel pore and surface diffusion model
Max. loading for the model (g/L column volume)	0.6, 1	6.5	20
Insulin of interest	Human, porcine, or LPI	Insulin and desamido	LPI, DP, and A21
Temperature (°C)	25	–[c]	15
Sorbent, particle radius, pore size	YMC-ODS-A, C18, 2.5 μm, 120 Å	Kromasil 100, C8, 5 μm, 110 Å	YMCbasic C8, 5 μm, 100 Å
Organic solvent, buffer, pH	MeCN, 0.1% TFA buffer	EtOH, CH_3COONH_4, pH 4	MeCN, 0.1 M morpholine, pH 7.8
φ	0.31 (v/v)	0.27, 0.28, 0.29, 0.30 (w/w)	0.19–0.40 (v/v)

[a] $q_i = \frac{a_i C_i}{[1+(b_i C_i)^m]^{1/m}}$, (the most heterogeneous sites) $0 \le m \le 1$ (homogeneous surface).

[b] $\frac{\partial q_i}{\partial t} = k_{kin,i}\left[H_i \times C_i\left(1 - \frac{q_I}{q_{\max,I}} - \frac{q_{dI}}{q_{\max,dI}}\right) - q_i\right]$, $H_i = b \times q_{\max} = H_{0,i} \times e^{\gamma\varphi}$.

[c] Not reported.

at 10 organic fractions, one would need more than 150 frontal experiments. A new method, which requires an order of magnitude fewer experiments and less material than the frontal method, is developed in this study to estimate both linear and nonlinear isotherm parameters over a wide range of organic fractions. The solvent-modulated linear isotherm parameters are estimated using small pulse linear gradient elution with different slopes, which probe the isotherm over a wide range of organic fractions. The solvent-modulated nonlinear isotherm parameters are estimated from frontals at three organic fractions. Strategies are also developed to estimate pore diffusivity and surface diffusivity using pulses and frontal tests. The estimated parameters are further verified by frontal, isocratic pulses, and large loading stepwise elution and linear gradient elution runs.

The results show that LPI and impurities are eluted when the ratios of pore diffusion flux to surface diffusion flux are between 0.1 and 10. Within this region, a parallel pore and surface diffusion model can predict closely the breakthrough curves and the elution profiles over a wide range of organic fractions (0.19–0.40), LPI concentrations (0.05–18 g/L), loading volume (0.0004–13 CV), and interstitial velocities (<10 cm/min). High product purity (>99.5% LPI) and high yield (≥95%) are obtained from stepwise and linear gradient elution. The experimental yield values for a desired LPI purity (>99.5%) are predicted to within ±1% by the model.

2. Theory

2.1. Parallel pore and surface diffusion model

Berninger et al. developed a pore diffusion model for multicomponent chromatography [18]. This model takes into account convection, axial dispersion, film mass transfer, pore diffusion, and competitive equilibrium or nonequilibrium adsorption/desorption. The pore diffusion model has been verified with various solutes in batch chromatography [14,19–31], carousel [27,32], and simulated moving bed [26,33–48]. The pore diffusion model, however, cannot predict asymmetric breakthrough curves of high affinity solutes. Ma et al. expanded the pore diffusion model to a parallel pore and surface diffusion model, which accounts for pore diffusion, surface diffusion, or parallel pore and surface diffusion [14]. We summarize below the key assumptions and model equations for the parallel pore and surface diffusion model. More detailed derivation can be found in Ma et al. [14].

The key assumptions of the model include: (a) uniformly packed column with uniform particle size and pore size; (b) uniform flow distribution in the column; (c) isothermal processes; (d) negligible radial dispersion and radial concentration gradients in the column; (e) only radial concentration gradient in particles; (f) incompressible mobile phase; and (g) constant pore and surface diffusivities. With these assumptions, the following dimensionless equations can be derived from differential mass balances, boundary conditions, and initial conditions for the i-th component in the bulk, pore, and solid phases [14]:

Bulk phase:

$$\frac{\partial c_{b,i}}{\partial \theta} = \frac{1}{Pe_{b,i}}\frac{\partial^2 c_{b,i}}{\partial x^2} - \frac{\partial c_{b,i}}{\partial x} - N_{f,i}(c_{b,i} - c_{p,i}|_{\xi=1}) \tag{1a}$$

$$x = 0, \quad \frac{\partial c_{b,i}}{\partial x} = Pe_{b,i}(c_{b,i} - c_{f,i}(\theta)) \tag{1b}$$

$$x = 1, \quad \frac{\partial c_{b,i}}{\partial x} = 0 \tag{1c}$$

$$\theta = 0, \quad c_{b,i} = c_{b,i}(0, x) \tag{1d}$$

Pore phase:

$$\varepsilon_p\left(\frac{\partial c_{p,i}}{\partial \theta}\right) = \frac{N_{p,i}}{\xi^2}\frac{\partial}{\partial \xi}\left(\xi^2\frac{\partial c_{p,i}}{\partial \xi}\right) - \frac{Y_{l,i}}{\phi_{L,i}} \tag{2a}$$

$$\xi = 0, \quad \frac{\partial c_{p,i}}{\partial \xi} = 0 \tag{2b}$$

$$\xi = 1 \quad N_{p,i}\frac{\partial c_{p,i}}{\partial \xi} + \frac{N_{s,i}}{\phi_{L,i}}\left(\frac{\partial \bar{c}_{p,i}}{\partial \xi}\right) = B_{f,i}(c_{b,i} - c_{p,i}) \tag{2c}$$

$$\theta = 0, \quad c_{p,i} = c_{p,i}(0, \xi) \tag{2d}$$

The boundary condition of Eq. (2c) is derived from a mass balance on a control surface at $r = R$. Since no mass accumulates on the control surface, at $r = R$, the film mass transfer flux from the bulk phase to the pore phase is equal to the sum of pore and surface diffusion fluxes into the particle [14].

Solid phase:

$$\frac{\partial \bar{c}_{p,i}}{\partial \theta} = \frac{N_{s,i}}{\xi^2}\frac{\partial}{\partial \xi}\left(\xi^2\frac{\partial \bar{c}_{p,i}}{\partial \xi}\right) + Y_{l,i} \tag{3a}$$

$$\xi = 0, \quad \frac{\partial \bar{c}_{p,i}}{\partial \xi} = 0 \tag{3b}$$

$$\xi = 1, \quad \frac{\partial \bar{c}_{p,i}}{\partial \theta} = 2N_{s,i}\frac{\partial \bar{c}_{p,i}}{\partial \xi} + Y_{l,i} \tag{3c}$$

$$\theta = 0 \quad \bar{c}_{p,i} = \bar{c}_{p,i}(0) \tag{3d}$$

The derivation of Eq. (3c) and a more detailed explanation can be found in the Appendix A of Ma et al. [14]. Eq. (3c) is derived from the unsteady state mass balance of species i in the solid phase in a thin layer of control volume between R and $(R - \Delta R)$. This control volume cannot be reduced to zero (or $\Delta R = 0$). Otherwise the net adsorption per solid volume ($Y_{l,i}$) and the accumulation term will be zero, resulting in no surface diffusion flux at the particle surface. Aris [49] and Riekert [50] proposed another boundary condition: $\partial \bar{c}_{p,i}/\partial \xi = 0$ at $\xi = 1$, which implies no surface diffusion can occur at the particle surface and contradicts Eq. (2c). Do and Rice proposed the other boundary condition: $\partial \bar{c}_{p,i}/\partial \theta = Y_{l,i}$, at $\xi = 1$ [51]. This boundary condition also implies no surface diffusion flux at the particle surface. Eq. (3c) is the only boundary condition that allows the general rate model to consider three separate cases with three different diffusion mechanisms: (1) pore diffusion, (2) surface diffusion, or (3) parallel pore and surface diffusion.

The solute concentrations in bulk phase C_b, pore phase C_p, solid phase $\bar{C}_p$ (based on solute adsorbed per solid volume), and feed solution C_f, are normalized by their respective maximum values:

$$c_{b,i} \equiv \frac{C_{b,i}}{C_{e,i}}; \quad c_{p,i} \equiv \frac{C_{p,i}}{C_{e,i}}; \quad \bar{c}_{p,i} \equiv \frac{\bar{C}_{p,i}}{\bar{C}_{T,i}}; \quad c_{f,i} \equiv \frac{C_{f,i}}{C_{e,i}} \tag{4}$$

where C_e is the maximal possible inlet concentration or a reference concentration, and $\bar{C}_T$ is the maximal capacity per solid volume. The definitions of the dimensionless groups can be found in 'Nomenclature'.

When the adsorption and desorption rates are faster than the controlling mass transfer rate, local equilibrium can be achieved between the solid and pore phases. The net adsorption rate of species i per solid volume, $Y_{l,i}$, for a local equilibrium system is defined as:

$$Y_{l,i} \equiv \sum_{j=1}^{N}\left[\frac{\partial \bar{c}_{p,i}}{\partial c_{p,j}}\frac{\partial c_{p,j}}{\partial \theta}\right] + \frac{\partial \bar{c}_{p,i}}{\partial \varphi}\frac{\partial \varphi}{\partial \theta} \tag{5}$$

where φ is the modulator concentration. When the adsorption and desorption rates are relatively slow compared to the controlling mass transfer, the assumption of local equilibrium is no longer

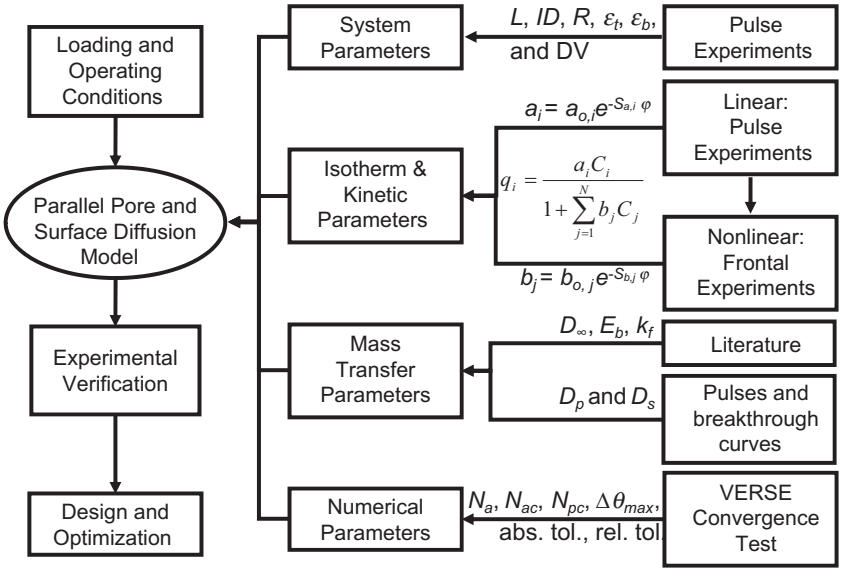

Fig. 1. Parallel pore and surface diffusion model and estimation of model parameters.

valid. The kinetic equation can relate the solid phase concentrations to the pore phase concentrations, as discussed later in Section 2.2.

The partial differential equations and associated boundary and initial conditions are discretized by orthogonal collocation on finite elements. The resulting ODE's and algebraic equations are solved using an equation solver. More details about the algorithm and the integration routine can be found in Berninger et al. [18].

The rate model requires input parameters, which include system, operating, isotherm, mass transfer, and numerical parameters (Fig. 1). The system parameters are related to the specific features of the equipment, such as column length (L), column inner diameter (ID), particle radius (R), column voidages (ε_t and ε_b), and system dead volume (DV). The column voidages and system dead volume can be measured by pulse or frontal experiments reported in Section 3.3.3. The operating parameters specify the loading volume, feed concentration and composition, linear velocity, organic modifier concentration, and gradient shape. The isotherm model and a strategy to estimate isotherm parameters are discussed in Section 2.2. A strategy to estimate pore diffusivity and surface diffusivity is proposed in this study (Section 2.4). Axial dispersion and film mass transfer parameters are estimated from literature correlations (Section 4.6). The numerical parameters are discussed in Section 4.2.

2.2. Modified reversed phase modulator isotherm (modified RPM)

The adsorption isotherms, which describe how the solute concentration in the stationary phase is related to that in the solution at equilibrium, strongly depend on the organic fraction in the mobile phase in RPC. The interactions between the adsorbent and the proteins are weakened with increasing organic fraction. This relation is incorporated into the isotherms using an exponential function of φ and tested for LPI and two impurities in RPC for the first time. The amount of the i-th component adsorbed per column packing volume, q_i, is given by

$$q_i = \frac{a_{o,i} e^{-S_{a,i}\varphi_e} C_{p,i}}{1 + \sum_{j=1}^{N} b_{o,j} e^{-s_{b,j}\varphi_e} C_{p,j}} \tag{6a}$$

where q_i is related to $\bar{C}_{p,i}$ by $q_i = (1-\varepsilon_t)\bar{C}_{p,i}$, C_p is the solute concentration in pore phase, S_a and S_b are the modulation parameters, N is the number of solutes in the system, and a_o and b_o are respectively the linear and nonlinear Langmuir isotherm parameters at a reference φ ($\varphi_{\text{reference}}$). In this study, the $\varphi_{\text{reference}}$ was chosen to be 0.19. Preliminary study indicated that LPI loaded could be fully recovered, when the column was pre-equilibrated at $\varphi = 0.19$ and the loading volume was kept below 5 CV. For this reason, the separations in this study were carried out at a loading $\varphi = 0.19$ and elution $\varphi > 0.19$. An effective φ, φ_e, which was defined as $\varphi_e = \varphi - 0.19$, instead of the actual φ was used in the simulations for two reasons: (1) the isotherm parameters for the rate model simulations were needed only when $\varphi \geq 0.19$, and (2) this shift in φ saves computation time for simulations. If the isotherm parameters were expressed as a function of φ, $a(\varphi)$, LPI would have very high linear isotherm a_o value ($>10^9$), which is the "a" value at $\varphi = 0$. Simulations using the "modified isotherms" with a large a_o value give the same results as those using the "modified isotherm parameters", $a(\varphi_e)$, but require more computation time.

The reversed phase modulator model reported in the literature assumed S_a and S_b are the same [52,53]. In this study, we found that different S_a and S_b values are needed to model LPI accurately. The well-known multi-component Langmuir isotherm is a special case of Eq. (6a) with a fixed φ_e value.

The nonequilibrium form of the modified reversed phase modulator isotherm is defined as:

$$Y_{l,i} \equiv \frac{\tau}{C_{T,i}} \left[l_{+,i}(\varphi_e) C_{p,i} \bar{C}_{T,i} \left[1 - \sum_{j=1}^{N} \frac{\bar{C}_{p,j}}{e^{-S_{+j}\varphi_e} \bar{C}_{T,j}} \right] - l_{-,i}(\varphi_e) \bar{C}_{p,i} \right] \tag{6b}$$

$$l_{+,i}(\varphi_e) = l_{o+,i} e^{-S_{+,i}\varphi_e} \tag{6c}$$

$$l_{-,i}(\varphi_e) = l_{o-,i} e^{S_{-i}\varphi_e} \tag{6d}$$

where $l_{o+,i}$ and $l_{o-,i}$ are respectively the intrinsic adsorption rate constant and desorption rate constant of the i-th component; S_+ and S_- are the solvent modulation parameters. The kinetic parameters can be related to the isotherm parameters for an equilibrium system according to the equations below:

$$\frac{l_{o+,i}}{l_{o-,i}} = b_{o,i} \tag{6e}$$

$$\bar{C}_{T,i}(1-\varepsilon_t) = \frac{a_{o,i}}{b_{o,i}} \tag{6f}$$

$$S_{b,i} = S_{-,i} \tag{6g}$$

$$S_{a,i} - S_{b,i} = S_{+,i} \tag{6h}$$

When $S_a = S_b$, $S_{+,i} = 0$ and the exponential term in Eq. (6b) will be 1 [23]. Eq. (6b) can also be expressed in terms of dimensionless groups:

$$Y_{l,i} \equiv N_{l+,i}(\varphi_e)c_{p,i}\left[1 - \sum_{j=1}^{N}\frac{\bar{c}_{p,j}}{e^{-S_{+,j}\varphi_e}}\right] - N_{l-,i}(\varphi_e)\bar{c}_{p,i} \tag{7a}$$

$$N_{l+,i}(\varphi_e) = \frac{C_{e,i}Ll_{+,i}(\varphi_e)}{u_0} \tag{7b}$$

$$N_{l-,i}(\varphi_e) = \frac{Ll_{-,i}(\varphi_e)}{u_0} \tag{7c}$$

where $N_{l+,i}$ is a characteristic adsorption rate relative to the convection rate, and $N_{l-,i}$ is a characteristic desorption rate relative to the convection rate [23].

2.2.1. Estimation of linear isotherm parameters using linear solvent strength theory (LSS)

The linear isotherm parameters in Eq. (6a) (a_o and S_a) can be estimated from the retention times of two or more pulses in linear gradient elution [54]. The capacity factor of component i at φ_e, $k_i(\varphi_e)$, which is proportional to $a_i(\varphi_e)$, can be related to φ_e:

$$k_i(\varphi_e) = k_{o,i}10^{-S_i\varphi_e} \tag{8}$$

where $k_{o,i}$ is the capacity factor of component i when the organic fraction $\varphi = \varphi_{\text{reference}} = 0.19$, and S_i is a constant for component i and a given organic modifier.

If the retention of a solute follows Eq. (8), the gradient elution time of the solute in a differential pulse, t_{GR}, is given as [54–58]:

$$t_{GR,n} = \left(\frac{t_0}{\beta_n}\right)\log(2.3k_o\beta_n + 1) + t_0 + t_d \tag{9a}$$

where

$$\beta_n = \frac{St_0(\varphi_{ef} - \varphi_{e0})}{T_{G,n}} \tag{9b}$$

where t_0 is the retention time of the solvent (or a non-adsorbing solute) in the column, β is the gradient steepness parameter, t_d is the time to fill extra-column dead volume, φ_{ef} is the effective organic fraction at the end of the linear gradient, φ_{e0} is the effective organic fraction at the beginning of the linear gradient, k_o is the capacity factor at φ_{e0}, T_G is the gradient time, and subscript n is the property for the n-th run. For each component, at least two linear gradient elution runs at different gradient slopes are needed to estimate the two unknowns, k_o and S in Eq. (9).

The linear isotherm parameter in the modified reversed phase modulator, $a_{o,i}$ in Eq. (6a), is related to $k_{o,i}$, based on the solute movement theory [59]:

$$a_i(\varphi_e) = \varepsilon_t k_i(\varphi_e) = \varepsilon_t\left(\frac{t_{r,i}(\varphi_e) - t_0}{t_0}\right) \tag{10a}$$

or

$$a_{o,i} = \varepsilon_t k_{o,i} \tag{10b}$$

where ε_t is the total porosity of the column, and $t_{r,i}(\varphi_e)$ is the retention time of component i in isocratic elution at φ_e. The linear isotherm modulator parameter, $S_{a,i}$ in Eq. (6a) is related to S_i:

$$S_{a,i} = S_i\ \ln(10) = 2.3S_i \tag{11}$$

Once we have $a_{o,i}$ and $S_{a,i}$, the linear isotherm parameter of component i at organic fraction φ_e can be calculated by:

$$a_i(\varphi_e) = a_{o,i}e^{-S_{a,i}\varphi_e} \tag{12}$$

2.2.2. Frontal analysis and effective column capacity

Frontal analysis, FA, is considered the most reliable method for determining adsorption isotherms. It has also been applied to estimate the isotherm of insulin or its variants [11,12,15–17]. In frontal analysis, the amount of compound adsorbed can be calculated by the mass balance equation:

$$q = \frac{C \times (V_{br} - V_o)}{\text{CV}} \tag{13}$$

where q refers to the amount of compound adsorbed per column volume when in equilibrium with the concentration, C, V_{br} is the breakthrough volume corrected for the extra-column dead volume, V_o is the column void volume, and CV is the column packing volume.

However, the frontal analysis equation Eq. (13) does not consider a gradual loss of column capacity upon repeated loading. A small amount (<1%) of high molecular weight impurities in the feed adsorb irreversibly on the column, resulting in slow fouling, or a gradual decrease in effective column capacity upon repeated loading. The capacity factor k of anthracene was used in this study to track the effective column capacity or effective column length. To account for any capacity loss upon repeated loading and stripping, an effective column length for an old column, L_{old}, can be calculated by:

$$L_{old} = \frac{k_{old}}{k_{new}} \times L_{new} \tag{14}$$

where L_{new} is the column length of a fresh column, k is the capacity factor of anthracene, subscript *old* or *new* refers to an old column or a fresh column, respectively. When an old column was used in the frontal experiments, the amount of compound adsorbed per fresh column volume can be estimated from the ratio of k:

$$q = \frac{C \times (V_{br} - V_o)}{\text{CV}_{old}} = \frac{C \times (V_{br} - V_o)}{\text{CV}_{new} \times (k_{old}/k_{new})} \tag{15}$$

2.2.3. Estimation of nonlinear isotherm parameters

Traditional frontal analysis requires a large amount of feed materials and 150 experiments to obtain accurate linear and nonlinear isotherm parameters at 10 organic fractions. Such an approach is expensive for proteins or other valuable pharmaceuticals.

A new method, which requires less feed and a smaller number of experiments, is tested in this study. This method combines both linear solvent strength theory and frontal analysis. The linear isotherm parameters were first estimated based on the retention times of two or more small pulses in linear gradient elution (Section 2.2.1). Once the linear isotherm parameters at each φ are known, the nonlinear isotherm parameters can be estimated from three or more frontal runs at different φs. For the Langmuir-type isotherm ($q(\varphi_e) = a(\varphi_e)C/(1 + b(\varphi_e)C)$), the nonlinear isotherm parameter $b(\varphi_e)$ can be calculated when $q(\varphi_e)$, $a(\varphi_e)$, and C are known.

$$b(\varphi_e) = \frac{a(\varphi_e)}{q(\varphi_e)} - \frac{1}{C} \tag{16}$$

where the linear isotherm parameter, $a(\varphi_e)$, is estimated from the linear solvent strength theory (Eq. (9)) or the retention time of an isocratic pulse at φ_e, and the $q(\varphi_e)$ and C values are from frontal analysis (Eq. (13) or Eq. (15)). With $a(\varphi_e)$ and frontal data at three different φ_es, the nonlinear isotherm parameters, b_o and S_b, can then be estimated from a plot of $\ln b(\varphi_e)$ versus φ_e:

$$\ln b(\varphi_e) = \ln\ b_o - S_b\varphi_e \tag{17}$$

2.3. Apparent pore diffusivity ($D_{p,app}$) and apparent surface diffusivity ($D_{s,app}$) in a parallel pore and surface diffusion system

For a system with only pore diffusion, the pore diffusion flux (J_p) can be related to the pore phase concentration gradient using the Fick's law:

$$J_p = -D_p \frac{\partial C_p}{\partial r} \tag{18}$$

For a system with only surface diffusion, the surface diffusion flux (J_s) can also be related to surface concentration gradient using the Fick's law:

$$J_s = -D_s \frac{\partial \bar{C}_p}{\partial r} = -\frac{D_s}{(1-\varepsilon_t)} \frac{\partial q}{\partial r} = -\frac{D_s}{(1-\varepsilon_b)(1-\varepsilon_p)} \frac{\partial q}{\partial r} \tag{19a}$$

where $\bar{C}_{p,i}$ (based on per solid volume) is related to q_i (based on per bed volume) via $q_i/(1-\varepsilon_t) = q_i/((1-\varepsilon_b)(1-\varepsilon_p))$. When the system is in local equilibrium, the surface concentration gradient can be expressed as a function of pore phase concentration gradient ($\partial C_p/\partial r$) and the slope of the isotherm ($\partial q/\partial C_p$) for a single component system:

$$J_s = -\frac{D_s}{(1-\varepsilon_t)} \frac{\partial q}{\partial C_p} \frac{\partial C_p}{\partial r} \tag{19b}$$

In a nonlinear isotherm system ($bC_p \gg 1$), the flux J_s depends on ($\partial C_p/\partial r$) and the slope of the isotherm $\partial q/\partial C_p$. The surface flux decreases with increasing loading concentration for a Langmuir system, since $\partial q/\partial C_p$ decreases with increasing C_p. For this reason, if surface diffusion dominates, the low concentration portion of the breakthrough curve is sharp and the high concentration portion is broad, and the breakthrough curve shows the characteristic slow approach to saturation [14].

In the case of parallel pore and surface diffusion, the overall intraparticle diffusion flux (J_{total}) is:

$$\begin{aligned} J_{total} &= \varepsilon_p J_p + (1-\varepsilon_p) J_s \\ &= -\varepsilon_p D_p \frac{\partial C_p}{\partial r} - \frac{(1-\varepsilon_p) D_s}{(1-\varepsilon_b)(1-\varepsilon_p)} \frac{\partial q}{\partial r} \\ &= -\varepsilon_p D_p \frac{\partial C_p}{\partial r} - \frac{D_s}{(1-\varepsilon_b)} \frac{\partial q}{\partial r} \end{aligned} \tag{20}$$

The shape of the breakthrough curves is more complex and is explained below. When a single-component parallel pore and surface diffusion system is in local equilibrium, J_{total} can be related to $\partial C_p/\partial r$ with an apparent pore diffusivity ($D_{p,app}$) [14]. For a system with the Langmuir isotherm:

$$D_{p,app} = D_p + \frac{D_s}{\varepsilon_p(1-\varepsilon_b)} \frac{\partial q}{\partial C_p} = D_p + \frac{D_s}{\varepsilon_p(1-\varepsilon_b)} \frac{a(\varphi_e)}{(1+b(\varphi_e)C_p)^2} \tag{21a}$$

Similarly, one can relate J_{total} to $\partial q/\partial r$ with a $D_{s,app}$:

$$\begin{aligned} D_{s,app} &= D_s + \varepsilon_p(1-\varepsilon_b) \frac{D_p}{(\partial q/\partial C_p)} \\ &= D_s + \varepsilon_p(1-\varepsilon_b) \frac{\left(1+b(\varphi_e)C_p\right)^2}{a(\varphi_e)} D_p \end{aligned} \tag{21b}$$

For fixed ε_b and ε_p, $D_{p,app}$ and $D_{s,app}$ are functions of isotherm parameters, organic fraction, and pore concentration. When φ is high, adsorption is negligible and there is no surface diffusion. Only pore diffusion is important and a symmetric breakthrough curve is expected.

In the linear isotherm region ($b(\varphi_e)C_p \ll 1$), $D_{p,app}$ and $D_{s,app}$ are constant at a given φ. Therefore, a symmetric breakthrough curve at a given φ is expected, and one cannot tell pore diffusion from surface diffusion. Breakthrough curves can be predicted by a pore diffusion model, a surface diffusion model, or a parallel pore and surface diffusion model. However, $D_{p,app}$ and $D_{s,app}$ can vary with φ, and have opposite φ dependence. At a small φ, $a(\varphi_e)$ is large, $D_{p,app}$ can be larger than the intrinsic D_p because of the contributions from surface diffusion (Eq. (21a)). As φ increases, $a(\varphi_e)$ decreases and $D_{p,app}$ decreases accordingly. By contrast, at a low φ, $a(\varphi_e)$ is large and $D_{s,app}$ approaches D_s. As φ increases, $a(\varphi_e)$ decreases, contributions from pore diffusion increase, and $D_{s,app}$ increases accordingly (Eq. (21b)).

In the nonlinear region ($b(\varphi_e)C_p \gg 1$), $D_{p,app}$ and $D_{s,app}$ are both functions of pore concentration and φ. As a result, neither a pore diffusion model nor a surface diffusion model can describe the breakthrough curves over a wide range of φ's or concentrations for a parallel pore and surface diffusion system, as shown in Section 4.

2.4. Strategy to estimate the intrinsic pore diffusivity (D_p) and surface diffusivity (D_s)

According to Eq. (21a), D_p can be estimated from pulses or breakthrough curves at a high φ, where adsorption and surface diffusion are negligible. The estimation of D_s is more challenging, since D_s is usually one or two orders of magnitude smaller than D_p, and surface diffusion can easily be dominated by pore diffusion, as expected from Eq. (21). To estimate D_s directly, one should minimize contributions from pore diffusion by using pulse or frontal data at a low φ and a low concentration. However, pulses at low φ are difficult to detect, since LPI adsorbs strongly, and a small pulse can disperse to below the detection limit. Breakthrough curves at a low concentration and a low φ are also difficult to detect, because of a long retention time and a low signal. Alternatively, breakthrough curves at an intermediate φ, where contributions from pore diffusion and surface diffusion are comparable, can be used to estimate D_s. The low concentration portion of the breakthrough curves can be used to estimate $D_{p,app}$, whereas the high concentration portion can be used to estimate $D_{s,app}$. Since D_p is estimated from pulse tests at a high φ, D_s can be solved from the estimated $D_{p,app}$ using Eq. (21a) or from the estimated $D_{s,app}$ using Eq. (21b).

2.5. Pore diffusion flux and surface diffusion flux as a function of φ and C_p

If the isotherm parameters, D_p, and D_s are known, one can use the ratio of pore diffusion flux to surface diffusion flux to identify the range of φ's and C_p's in which pore diffusion dominates, surface diffusion dominates, or both pore and surface diffusion are important:

$$\frac{\varepsilon_p J_p}{(1-\varepsilon_p) J_s} = \frac{-\varepsilon_p D_p (\partial C_p/\partial r)}{-(D_s/(1-\varepsilon_b))(\partial q/\partial r)} \tag{22a}$$

For a system with the Langmuir-type isotherm:

$$\frac{\varepsilon_p J_p}{(1-\varepsilon_p) J_s} = \frac{-\varepsilon_p D_p (\partial C_p/\partial r)}{-(D_s/(1-\varepsilon_b))(\partial (aC_p/(1+bC_p))/\partial r)} \tag{22b}$$

The maximum concentration gradient at C_p is the concentration change from zero to C_p. Therefore, Eq. (22b) can be simplified to:

$$\frac{\varepsilon_p J_p}{(1-\varepsilon_p) J_s} = \varepsilon_p(1-\varepsilon_p) \frac{D_p}{D_s} \frac{C_p}{(aC_p/(1+bC_p))} = \varepsilon_p(1-\varepsilon_b) \frac{D_p}{D_s} \frac{(1+bC_p)}{a} \tag{22c}$$

For LPI, since a and b are functions of φ, Eq. (22c) becomes:

$$\frac{\varepsilon_p J_p}{(1-\varepsilon_p) J_s} = \varepsilon_p(1-\varepsilon_b) \frac{D_p}{D_s} \frac{(1+b(\varphi)C_p)}{a(\varphi)} \tag{22d}$$

If pore diffusion dominates, one would expect the ratio of pore diffusion flux to surface diffusion flux is much greater than 1 and Eq.

(22d) can be rearranged:

$$1 + b(\varphi)C_p >> \frac{a(\varphi)}{\varepsilon_p(1-\varepsilon_b)}\frac{D_s}{D_p} \quad (23a)$$

If surface diffusion dominates, one would expect the ratio of pore diffusion flux to surface diffusion flux is much smaller than 1 and

$$\frac{a(\varphi)}{\varepsilon_p(1-\varepsilon_b)}\frac{D_s}{D_p} - 1 >> b(\varphi)C_p \quad (23b)$$

3. Experimental

The solution preparation and pH measurements were carried out at 15 °C. All chemicals were equilibrated to 15 °C before preparation, and kept at 15 °C during the chromatography runs. All solutions were prepared based on weight, and were used within three days of preparation. The densities of the solutions were determined either experimentally at 15 °C or were taken from literature correlations [60].

3.1. Materials

Crude feed solutions for C8 reversed phase purification and LPI crystals for frontal analysis were provided gratis by Eli Lilly & Co. (Indianapolis, IN). The crude solutions had approximately 6–7 g/L of LPI, 0.06 g/L DP, and 0.01 g/L A21. All reagents used in these studies were reagent grade. Sodium 1-octanesulfonate and sodium acetate trihydrate were purchased from Sigma–Aldrich (St. Louis, MO). Morpholine and diethylamine were purchased from Fisher Scientific (Fair Lawn, NJ). Sodium sulfate anhydrous, acetonitrile, phosphoric acid, hydrochloric acid, and sodium hydroxide were purchased from Mallinckrodt Baker (Phillipsburg, NJ). Deionized water was obtained from a Millipore (Bedford, MA) four-stage cartridge system.

3.2. Equipment

An Agilent 1100 HPLC unit (Santa Clara, CA) consisting of a micro vacuum degasser, a binary pump, an autosampler with a maximum injection volume of 100 μL, a thermostatted autosampler, a thermostatted column compartment, a variable wavelength detector, and a Hewlett-Packard PC with Agilent ChemStation® software was used for the analytical and small loading semi-preparative operation. For loading volume greater than 100 μL, the Agilent 1100 HPLC unit was also used but instead of the autosampler, a manual injector valve (Rheodyne 7725i) was attached for feed injection and the feed solution was pumped with a Waters 515 pump (Milford, MA).

A Zorbax 300SB-C8 (3 mm × 100 mm, particle diameter of 3.5 μm, and pore diameter of 300 Å) analytical column and a Narrow Bore guard column (2.1 mm × 12.5 mm, 5 μm, 300 Å) were obtained from Agilent Technologies (Santa Clara, CA). A YMCbasic C8 semi-preparative column (10 mm × 150 mm, 10 μm, 100 Å) was obtained from Waters (Milford, MA). Regular column performance tests showed the column capacity remained stable throughout the experiments.

A Mettler Toledo AG204 or a Denver Instrument XL3100 balance and a ThermoOrion 420A pH meter were used in solution preparation. The sample temperatures of analytical and semi-preparative runs were 4 and 15 °C, respectively. For loading volume greater than 100 μL, the feed solutions were maintained at 15 °C in a Honeywell cooler (Princess International Inc., Brooklyn, NY). The column temperatures of analytical and semi-preparative runs were 25 and 15 °C, respectively. Analytical mobile phases were maintained at 25 °C in a water bath (Sheldon Manufacturing, Inc., Cornelius, OR). Mobile phases for the semi-preparative chromatography were maintained at 15 °C by a cold room (Bally Case and Cooler Inc., Bally, PA).

3.3. Procedures

3.3.1. Analytical HPLC procedure

The analytical HPLC assay was carried out on a narrow bore C8 guard column and a 300SB-C8 column in series at 25 °C with a 2 μL injection at 0.80 mL/min. The mobile phase was a mixture of acetonitrile and 0.035 M sodium phosphate (monobasic) buffer. Two linear gradients were applied; the first, from 0.37 to 0.40 MeCN fraction in 10.0 min, and the next, from 0.40 to 0.41 MeCN fraction in 5.0 min. For regeneration, a step-up to 0.50 MeCN fraction was applied for 2.2 min, before a 2.0 min re-equilibration back to the initial conditions. The chromatograms were examined at 215 nm wavelength. To ensure analytical accuracy, a feed sample was injected every 10 injections as a control. Reproducible retention time of the feed sample indicated consistent analytical column performance.

3.3.2. Sample preparation

The crude LPI solutions were kept in the freezer (−20 °C) and thawed before use. Morpholine and 10% (v/v) hydrochloric acid were kept at 4 °C and 10 °C, respectively. The crude LPI solution was thawed in a water bath (17–18 °C) for 30 min. After the feed was completely thawed, morpholine was added. The pH was adjusted to 7.6–8.0 with 10% hydrochloric acid at a temperature between 13 and 17 °C. Finally, acetonitrile was added to the pH adjusted solution such that the final solution had 0.1 M morpholine, desired MeCN fraction (v/v), and controlled pH (7.6–8.0). The feed solution was equilibrated to 15 °C for 30 min before injection. All feed solutions were used within 2 h after preparation.

Pure DP and pure A21 samples were prepared for the isotherm parameter estimation. Pure fractions of DP were collected from large loading (2–3 CV) semi-preparative runs. The purity and concentration of A21 obtained from the semi-preparative runs were too low for parameter estimation. To obtain A21 standards, LPI was first converted to A21 by adding HCl to pH about 2 [17,61]. The samples were incubated for about 3 days at 40 °C and then analyzed by HPLC. The A21 content was about 60% and was determined from the HPLC chromatograms.

3.3.3. System parameters

The extra-column dead volume was measured by a series of MeCN step change experiments (from $\varphi = 0.00$ to 0.05) at two different flowrates (0.3 and 0.5 mL/min) at 192 nm. Three trials were done for each flowrate, and the results were reproducible. The interparticle porosity of the semi-preparative column, ε_b, was measured with a series of 0.5 μL 0.1 g/L blue dextran (MW = 2,000,000) pulse injections at $\varphi = 0.80$. The response was monitored at 430 nm. Three trials were done for each superficial velocity (1.3 cm/min or 0.6 cm/min). The intraparticle porosity (ε_p) of the semi-preparative column was calculated from the packing density (ρ_b), solid density (ρ_s), and interparticle porosity (ε_b) ($\rho_b = (1-\varepsilon_b)(1-\varepsilon_p)\rho_s$).

3.3.4. Semi-preparative column performance

A regular column performance test was conducted between runs to track the efficiency and effective capacity of the semi-preparative columns. The procedure was adapted from the published instruction of the manufacturer. The standard for the semi-preparative column was 0.092 g/L uracil ($C_4H_4N_2O_2$, MW 112.09) and 0.024 g/L anthracene ($C_{14}H_{10}$, MW 178.23) in 0.60 (v/v) MeCN solution ($\varphi = 0.60$). The operating temperature was 15 °C. The semi-preparative column was equilibrated at $\varphi = 0.60$ at a flowrate of 3.0 mL/min for 2 CV. After a 20 μL sample was injected, isocratic elution at $\varphi = 0.60$ was carried out for 20 min. The chromatograms

Table 2
Operating conditions and mass balances of frontal experiments.

Run	F1	F2	F3	F4	F5	F6	F7
Column length, L (cm)[a]	14.2	15.0	15.0	14.2	15.0	15.0	15.0
MeCN fraction, φ	0.30	0.27	0.23	0.19	0.27	0.27	0.27
Load volume (CV)	8.9	6.8	13.3	16.1	4.4	3.0	3.0
[LPI] in feed (g/L)	4.8	3.7	5.3	5.7	11.1	18.1	22.7
Loading amount (g/CV)	42.6	25.1	70.5	91.4	48.6	54.4	68.1
Flowrate (CV/h)	4.5	7.3	4.6	4.9	11.0	10.6	10.0
Velocity, u_0 (cm/min)	4.1	6.7	4.3	4.5	10.1	9.8	9.3
Regeneration volume (CV)	2.2	4.0	2.3	1.3	6.0	7.2	10
φ at regeneration	0.6	0.6	0.6	0.6	0.6	0.6	0.6
Regeneration flowrate (CV/h)	5.6	12.0	4.6	2.6	12.1	12.0	12.0
Regeneration velocity, u_0 (cm/min)	5.2	11.1	4.3	2.4	11.2	11.1	11.1
LPI mass balance (out/in)	0.99	0.98	0.98	–[b]	0.95	0.97	0.95

[a] The effective column length is calculated from Eq. (14).
[b] The mass balance of F4 is unavailable.

were examined at 254 nm wavelength. The effective column length was calculated based on the capacity factors of anthracene and Eq. (14). A 100 μL LPI isocratic elution was performed at $\varphi = 0.28$ as an independent check for column performance.

3.3.5. Semi-preparative chromatography

Different types of semi-preparative runs on the YMCbasic C8 columns were conducted at 15 °C. The mobile phase consisted of a mixture of acetonitrile and 0.1 M morpholine buffer with pH adjusted to 7.6–8.0 by 10% (v/v) hydrochloric acid. To measure MeCN adsorption isotherm, the column was pre-equilibrated at a flowrate of 1.2 mL/min (1.53 cm/min) at $\varphi = 0.05$, 0.10, 0.15, 0.20, 0.25, or 0.30. A pure MeCN pulse (50 μL) was then injected to the pre-equilibrated column, and the pulse was monitored at 190 nm. The retention time was used to estimate MeCN isotherm parameters at different MeCN fractions. At least two replicate runs were tested at each φ to ensure reproducibility.

Small loading (100 μL or lower) linear gradient elution at 2.4 mL/min (11.3 cm/min) was used to estimate linear isotherm parameters for LPI and the two impurities. The small pulses were monitored at 280 nm, where the response was high. The column was first pre-equilibrated with at least 2 CV at the loading φ. A loading φ of 0.19 was used in the linear gradient elution runs. Two different MeCN ranges were tested in the linear gradient elution runs: from 0.19 to 0.43 MeCN fraction over 9, 18 and 27 CV, and from 0.19 to 0.35 MeCN fraction over 6, 12, and 18 CV. Small loading (100 μL) isocratic elution runs (at $\varphi = 0.27$, 0.28, and 0.30) were carried out to verify the linear isotherm parameters estimated from the linear gradient runs. Linear velocities tested in isocratic elution include 2.6, 5.5, and 11.3 cm/min. The column was regenerated at $\varphi = 0.60$ for at least 2 CV after each run.

Frontal and large loading (>100 μL) linear gradient and stepwise elution runs required the use of a feed pump. Large loading experiments were monitored at 295 nm, where the response was found to be linear over a wide range of concentrations. Each run was pre-equilibrated at $\varphi = 0.19$ before loading and later regenerated at $\varphi = 0.60$. Each pre-equilibration or regeneration step takes at least 2 CV of solution. The effluent was collected in fractions for HPLC analysis. The detailed loading and operating conditions of the large loading semi-preparative runs are summarized in Tables 2–4.

4. Results and discussion

4.1. Experimental mass balance of LPI in frontal runs and the yield of LPI for the stepwise elution and linear gradient elution runs

The mass balance of each frontal run was examined to see if the adsorbed LPI can be fully recovered when loaded at $\varphi = 0.19$ and 15 °C (Table 2). The mass balance of LPI was defined as the amount of LPI eluted relative to the amount of LPI loaded. The amount of LPI loaded was calculated from loading volume and feed concentration. The amount of LPI eluted was calculated based on the integrated peak area in the semi-preparative chromatogram.

The mass balance results (Table 2) indicate that most of the LPI (95% or greater) loaded in the frontal runs, except F4, was eluted. The difference between input and output was less than 5%, which was within the errors from HPLC analysis and integration of the peak areas of the semi-preparative chromatograms. For F4, column frits were clogged after 16 CV loading at 5.7 g/L and the mass balance was unavailable. The mass balances for large loading stepwise elution runs (Table 3) and linear gradient elution runs (Table 4) were also 95% or greater. The results indicate that all the LPI adsorbed at $\varphi = 0.19$ was recovered under the conditions tested. More important, for a product purity requirement of LPI ≥ 99.5%, DP ≤ 0.3%, and A21 ≤ 0.15%, the experimental yield of LPI was greater than 97% in the stepwise elution runs (S1 and S2) and greater than 95% in the linear gradient elution runs (L1 and L2).

Table 3
Operating conditions and mass balances of large loading stepwise elution runs.

Run	S1	S2	S3
Column length, L (cm)[a]	15.0	15.0	14.2
Load volume (CV)	3.3	2.0	2.0
[DP] in feed (g/L)	0.08	0.05	0.05
[LPI] in feed (g/L)	4.6	4.7	4.5
[A21] in feed (g/L)	0.06	0.004	0.02
Loading amount (g/CV)	15.3	9.4	9.1
Loading velocity, u_0 (cm/min)	7.0	7.0	5.6
Loading flowrate (CV/h)	7.6	7.4	6.1
MeCN fraction at step 1, φ_1	0.28	0.27	0.25
Elution volume at step 1 (CV)	3.4	3.5	7.2
MeCN fraction at step 2, φ_2	0.31	0.31	0.28
Elution volume at step 2 (CV)	1.7	1.4	1.3
Elution velocity, u_0 (cm/min)	5.6	4.8	5.6
Elution flowrate (CV/h)	6.2	5.2	6.1
$N_{p,app}$ (φ_1)	12	16	23
Regeneration volume (CV)	2.0	2.0	2.0
φ at regeneration	0.6	0.6	0.6
Regeneration velocity, u_0 (cm/min)	11.5	11.5	5.6
Regeneration flowrate (CV/h)	12.2	12.2	6.1
LPI mass balance (out/in)	1.01	0.99	1.00
Exp. purity (%)[b]	99.8	99.6	99.8
Exp. yield (%)[b]	97.0	97.3	94.6
$C_{product}$ (g/L)	5.1	3.4	3.7
Productivity (g/L h^{-1})	6.3	5.0	3.8
Sim. purity (%)[b]	99.5	99.6	99.5
Sim. yield (%)[b]	89.3	98.2	98.4

[a] The effective column length is calculated from Eq. (14).
[b] The product purity requirements are: LPI ≥ 99.5%, DP ≤ 0.3%, A21 ≤ 0.15%.

Table 4
Operating conditions and mass balances of large loading linear gradient elution runs.

Run	L1	L2	L3	L4
Column length, L (cm)	15	15	15	15
Load volume (CV)	2.7	2.4	4.2	4.2
[DP] in feed (g/L)	0.07	0.08	0.05	0.06
[LPI] in feed (g/L)	5.8	6.3	4.5	4.4
[A21] in feed (g/L)	0.01	0.01	0.01	0.01
Loading amount (g/CV)	15.6	15.0	18.8	18.4
Loading velocity, u_0 (cm/min)	5.9	5.0	12.0	12.8
Loading flowrate (CV/h)	6.4	5.4	13.0	13.8
φ_0 at the beginning of elution	0.22	0.22	0.19	0.19
φ_f at the end of elution	0.31	0.33	0.35	0.37
Elution slope (%/CV)	0.87	1.43	0.92	2.19
Elution velocity, u_0 (cm/min)	3.0	3.1	10.9	10.0
Elution flowrate (CV/h)	3.3	3.4	11.8	10.9
$N_{p,app}$ (φ = 0.27)	26	23	7	7
Regeneration volume (CV)	2.0	2.0	2.0	2.0
φ at regeneration	0.6	0.6	0.6	0.6
Regeneration velocity, u_0 (cm/min)	6.3	3.1	10.9	10.9
Regeneration flowrate (CV/h)	6.8	3.4	11.8	11.8
LPI mass balance (out/in)	1.0	1.0	0.95	0.95
Exp. purity (%)[a]	99.5	99.5	–	–
Exp. yield (%)[a]	94.6	94.6	–	–
$C_{product}$ (g/L)	5.6	9.7	–	–
Productivity (g/L h^{-1})	3.5	4.3	–	–
Sim. purity (%)[a]	99.6	99.7	–	–
Sim. yield (%)[a]	96.9	95.5	–	–

[a] The product purity requirements are: LPI ≥ 99.5%, DP ≤ 0.3%, A21 ≤ 0.15%.

4.2. Numerical parameters and mass balance of simulations

To ensure the convergence of numerical solutions, simulations were carried out to check each of the six numerical parameters, including number of axial elements (N_a), number of axial collocation points (N_{ac}), number of particle collocation points (N_{pc}), absolute tolerance, relative tolerance, and integration step time ($\Delta\theta_{max}$). In this study, a numerical solution was considered converged when simulations were identical when N_a, N_{ac}, and N_{pc} were increased and absolute tolerance, relative tolerance, and $\Delta\theta_{max}$

Table 5
Parameters of the parallel pore and surface diffusion model used in VERSE simulation.

System parameters	L [a] (cm)	ID (cm)	R (μm)	ε_b	ε_p	Dead Volume (%CV)
	15	1	5	0.27	0.67	0.6 (≤ 100 μL pulse); 7 (frontal and > 100 μL loading)

Mass transfer parameters	k_f (cm/min)	Wilson and Geankoplis (1966)			
	E_b (cm^2/min) [b]	Chung and Wen (1968)			
	Component / Parameter	MeCN	DP	LPI	A21
	D_∞ (cm^2/min)	7.3×10^{-4}	5.2×10^{-5}	5.2×10^{-5}	5.2×10^{-5}
	D_p (cm^2/min)	2.1×10^{-5}	1.5×10^{-6}	1.5×10^{-6}	1.5×10^{-6}
	D_s (cm^2/min)	–	–	1.7×10^{-7}	–
	Ke (–)[c]	1	1	1 (0.75)	1
Isotherm parameters [c]	a_o (CV basis)	0	1438	2172 (2172)	5147
	S_a (–)	0	80	78 (76)	80
	b_o (L/g)	0	0	34 (32)	0
	S_b (–)	0	0	71 (70)	0
Numerical parameters	Absolute tolerance (g/L)	10^{-4}	10^{-6}	10^{-4}	10^{-6}
	Relative tolerance	10^{-3}	10^{-4}	10^{-3}	10^{-4}
	Number ofaxial elements	Integration step size ($\Delta\theta_{max}$) (% CV)	Collocation points: Axial	Particle	
	400	0.1	4	1	

[a] The column length of a fresh column was 15 cm. Depends on the column usage, an effective column length was used in the simulations.
[b] An empirical equation ($E_b \propto u_0$) is tested to describe the long tailing at high elution velocities (u_0 > 10 cm/min).
[c] The isotherm parameters are based on φ_e (=φ – 0.19). The isotherm parameters in parentheses for LPI were based on Ke of 0.75. Others are based on Ke of 1. The two sets of isotherm parameters are equivalent. More detailed derivation and discussion are given in Appendix A.

were reduced. Since the impurities were a hundred times smaller than LPI in concentration, the tolerance values set for impurities were smaller than those for LPI. Table 5 summarizes the numerical parameters used to obtain converged solutions in this study. The mass balance errors of the simulations were within ±1%, which was within the tolerances set for the computation.

4.3. MeCN adsorption

If an organic modifier is adsorbed on a RPC column, it can compete with proteins for the adsorption sites. The adsorption can also affect gradient shape. MeCN adsorption on a C8 column was observed when a pulse of MeCN was injected into a C8 column which was pre-equilibrated at $\varphi = 0.05$ (or 39 g/L). To obtain the MeCN adsorption isotherm, the column was equilibrated at $\varphi = 0.05$, 0.10, 0.15, 0.20, 0.25, 0.30, and 0.40 (or 315 g/L). At each φ, a pulse of pure MeCN was injected to obtain the retention time, which was used to find the slope of the isotherm ($\partial q/\partial\varphi$) at φ. The slopes at the seven φ values were correlated with a third order polynomial equation, which was integrated to find $q(\varphi)$.

The standard Langmuir isotherm was tested to correlate the MeCN adsorption data. The linear and nonlinear isotherm parameters were respectively 0.164 and 0.002 ($q_{MeCN} = 0.164\,C_{MeCN}/(1 + 0.002\,C_{MeCN})$). The units of C_{MeCN} and q_{MeCN} were grams per liter column volume (g/L) in the Langmuir isotherm. When the concentration of MeCN increased from 150 to 315 g/L (corresponding to φ from 0.19 to 0.40), the concentration of MeCN adsorbed increased from 20 to 33 g/L. Only 0.15 g of MeCN uptake was needed to change column presaturation from $\varphi = 0.19$ to 0.40 for the semi-preparative column (12 mL). The small amount of MeCN adsorption has negligible effect on gradient shape in the range studied. VERSE simulations were conducted to check this assumption. As expected, the resulting outlet gradient shapes were identical in the absence and in the presence of MeCN adsorption. The effect of competitive adsorption of MeCN with LPI was lumped with the modulation effects of MeCN and taken into account by the modulator constants, S_a and S_b, in the LPI isotherm as shown below.

4.4. Linear isotherm parameters

4.4.1. Estimation of linear isotherm parameters (a_o and S_a)

Linear isotherm parameters, a_o and S_a, were estimated from the retention times of 27 linear gradient elution runs by applying Eq. (9). Small pulse linear gradient elution runs with different gradient slopes were carried out for each of the key components: DP, LPI, and A21. Mass-center retention data of 100 μL (~0.01 CV) injections and gradients of MeCN fraction from 0.19 to 0.35 over 6, 12, or 18 CV were used in Eq. (9) to estimate the linear isotherm parameters. To test whether a wider range of φ's and a smaller pulse size could improve the accuracy of the isotherm parameters, pulse injections (5 μL, 0.0004 CV) with the same gradient slopes but over a wider φ range were carried out (φ from 0.19 to 0.43 over 9, 18, or 27 CV) (Fig. 2). Two or more replicate runs were done to ensure reproducibility. The isotherm parameters estimated from the two sets of linear gradient elution data were in close agreement. Differences in the MeCN range and pulse size had negligible effect on the estimated linear isotherm parameters.

The linear gradient elution data provided estimation of linear isotherm parameters of LPI and the two impurities over a wide range of φ's. Only the linear isotherm parameters in a high organic fraction ($\varphi \geq 0.24$) range could be verified using isocratic elution of small pulses (6.0 g/L LPI, 100 μL, ~0.01 CV). At a lower organic fraction ($\varphi < 0.24$), a pulse in isocratic elution had a retention time of more than 6 h and the eluted pulse was too dispersed to be detected. Isocratic elution runs with duplicate small pulses at $\varphi = 0.27$, 0.28, and 0.30 were carried out (Fig. 3). The linear isotherm parameters "a" estimated from the isocratic elution runs were in close agreement with the correlation "a" as a function of φ obtained from the linear gradient elution (Fig. 4a). The linear parameters of this correlation based on φ_e are shown in Table 5.

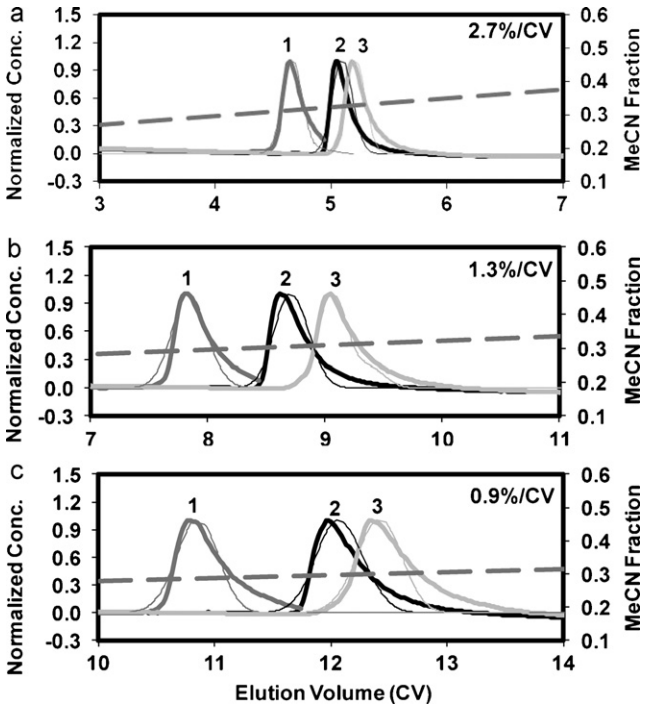

Fig. 2. Small pulse (5 μL for LPI, 100 μL for DP and A21) linear gradient elution runs from 0.19 to 0.43 MeCN fractions over: (a) 9 CV, (b) 18 CV, and (c) 27 CV for each of the key components. For comparison, the concentrations are normalized by the maximum peak concentration. Thick lines are UV traces at 280 nm. Thin lines are simulations based on the pore diffusion model. Dashed lines are simulated outlet MeCN fraction. Peaks 1–3 are DP, LPI, and A21, respectively. *Note*: The pulse data of DP, LPI, and A21 are superimposed in one plot. The interstitial velocity of these runs is 11.3 cm/min. The elution volume (x-axis) does not include dead volume.

The LPI pulses in isocratic elution at $\varphi = 0.6$ show that LPI had no adsorption and was slightly excluded from the pores. A size exclusion factor (Ke) for LPI of 0.75 can explain the peak profile (Fig. 3a). Effective isotherm parameters for LPI were first calculated by assuming a size exclusion factor (Ke) of 1 (Table 5). The effect of size exclusion was lumped into the effective adsorption parameters. A second set of isotherm parameters for LPI was calculated based on the size exclusion factor of 0.75 (Appendix A) and reported in parenthesis in Table 5. The derivation and the relation of the two sets of isotherm parameters are reported in Appendix A. The two sets gave essentially the same $a(\varphi_e)$, except when $\varphi > 0.4$ ($a(\varphi_e) < 0.001$, see Supplementary Fig. A). For this reason, the isocratic elution pulse at $\varphi = 0.6$ (no adsorption) can be better explained by the second set of isotherm parameters with the size exclusion factor of 0.75 (Fig. 3a). The two sets of isotherm parameters gave the same simulation results for all the other runs. The results indicate that the effective isotherm parameters for LPI gave accurate results when $\varphi < 0.4$.

4.4.2. Verification of linear isotherm parameters

To verify the linear isotherm parameters of LPI and the impurities, the pore diffusion model was tested to simulate the profiles of linear gradient elution, from which the retention times were used in estimating the linear isotherm parameters ($a(\varphi_e)$). The system dead volume for pulse injections was about 0.3 mL which was estimated using pulse tests without the column attached. The dead volume was treated as two CSTR volumes: one CSTR (0.15 mL) before the

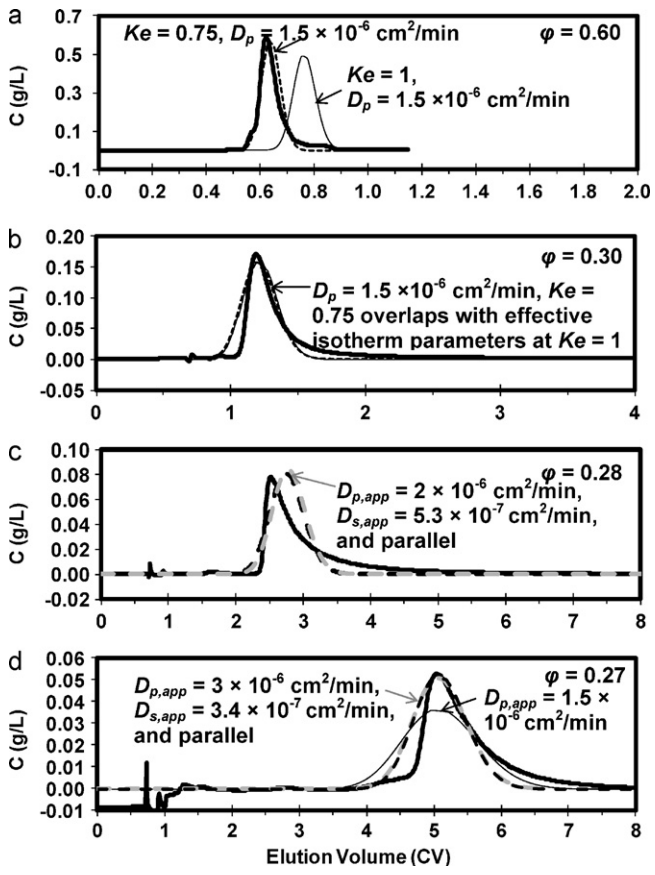

Fig. 3. Small pulse (100 μL, ~0.01 CV loading) LPI isocratic elution runs at different MeCN fractions: (a) 0.60, (b) 0.30, (c) 0.28, and (d) 0.27. (—) UV traces at 280 nm. All predictions are based on the the effective isotherms at $Ke = 1.0$ except the dashed curves in (a) and (b), which are based on the pore diffusion model with the intrinsic isotherm parameters at $Ke = 0.75$. Thin solid lines are predictions of the pore diffusion model ($D_p = 1.5 \times 10^{-6}$ cm^2/min). The predictions of the three models (pore diffusion, surface diffusion, and parallel diffusion) overlap in (c) and (d). The interstitial velocity of these runs is 11.3 cm/min.

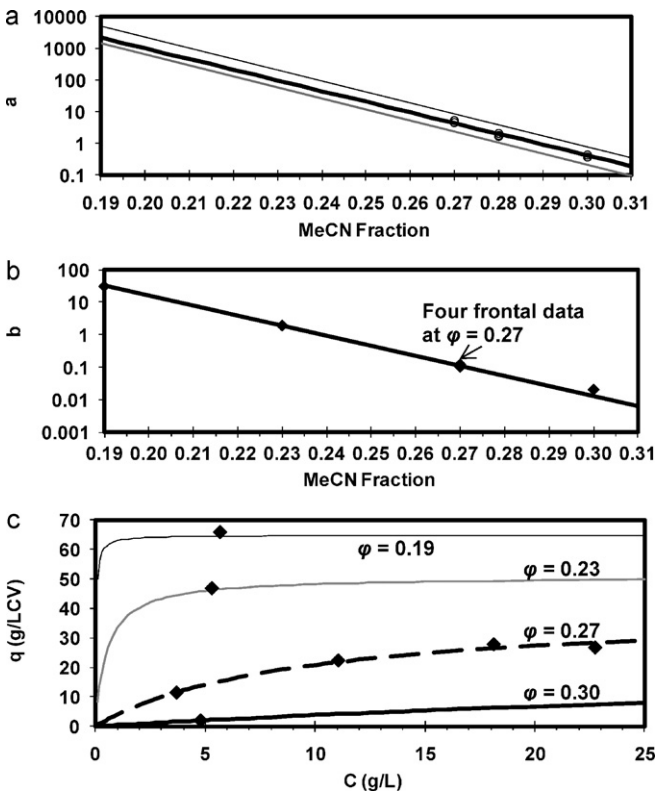

Fig. 4. Modified reversed phase modulator isotherm and model parameters of LPI and impurities as a function of MeCN fraction: (a) linear isotherm parameters. Symbols (○) were estimated from 100 mL isocratic LPI pulses. Lines were estimated from pulse linear gradient elution runs: (▬) DP, (—) LPI, and (——) A21, (b) Nonlinear isotherm parameters of LPI: (♦) frontal data and (—) model prediction, (c) modified reversed phase modulator isotherm for LPI.

column and one after the column in the simulations. The simulations closely predicted the peak retention times (mass center) of the small pulse data (Figs. 2 and 3). Note that the *x*-axis is the net elution volume where the system dead volume is subtracted from the elution volume. The linear isotherm parameters were further verified with frontal runs, large loading stepwise elution, and large loading linear gradient elution runs, as discussed in Sections 4.6.2 and 4.7.2.

4.5. Estimation of nonlinear isotherm parameters (b_o and S_b)

In this study, the nonlinear isotherm parameters of LPI were estimated from frontals at three organic fractions ($\varphi = 0.27$, 0.23, and 0.19 (F2, F3, and F4)) at feed concentration from 3.7 to 5.7 g/L (Table 2 and Fig. 5). At $\varphi > 0.27$, the nonlinear isotherm parameter was too small ($b < 0.1$ L/g) to be measured accurately by this method. The frontal data at $\varphi = 0.3$ (F1) were not included in the estimation of "*b*" (Fig. 5a). Instead, F1 was used to verify the parameters estimated from the other three frontals. Fig. 4b plots the nonlinear isotherm parameters of LPI (*b*) as a function of φ. Fig. 4c summarizes the amount of LPI adsorbed per bed volume as a function of φ and protein concentration.

To check whether the "*b*" values obtained in the three frontal runs were valid at different feed concentrations, three additional frontal experiments with 11.1, 18.1, and 22.7 g/L LPI in the feed solutions were carried out at $\varphi = 0.27$ (F5, F6, and F7 in Table 2). The nonlinear isotherm parameter, *b*, at $\varphi = 0.27$ calculated from the three runs was 0.11 ± 0.01 L/g, which agreed closely with the model parameters estimated from F2, F3, and F4 (Fig. 4b and c). The results indicate that the frontal experiments at three different φ are sufficient to estimate the nonlinear isotherm parameters.

Since the impurities had at least 100 times lower concentrations than LPI, the nonlinear terms in the modified reversed phase modulator, $b_j C_j$, of the two impurities were negligible in Eq. (6a). The nonlinear isotherm parameters of the impurities were set to zero in the simulations. The nonlinear isotherm parameters of LPI were needed for accurate predictions of LPI and the two impurities in large loading (≥2 CV) stepwise and linear gradient elution runs. Table 5 summarizes the isotherm parameters of LPI and the impurities used in the simulations.

The effective capacity of the semi-preparative columns was estimated using anthracene pulse tests throughout their use to detect any loss of capacity due to column fouling. A pulse injection of a mixture of uracil and anthracene for column characterization was done before and after each frontal experiment. The ratio of the capacity factor of the anthracene was substituted into Eq. (14) to calculate the effective column length. Two fresh columns were used for the frontal runs at $\varphi = 0.23$ and 0.27, respectively. A 5% decrease in the effective column length was used to take into account the capacity loss in subsequent runs for $\varphi = 0.19$ and 0.30.

4.6. Mass transfer parameters

4.6.1. Estimation of mass transfer parameters

A parallel pore and surface diffusion model was tested for LPI and the two impurities. Since the molecular structures of the impu-

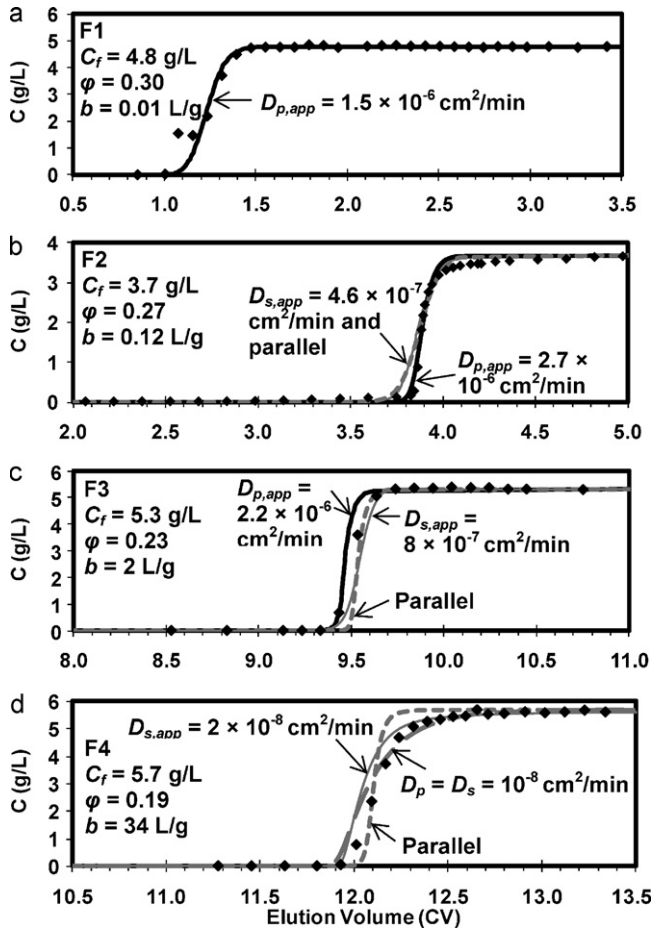

Fig. 5. LPI frontal experiments at different MeCN fractions: (a) F1, (b) F2, (c) F3, and (d) F4. (♦) HPLC results of LPI; lines are predictions based on the parameters in Table 5: (▬) pore diffusion model, (——) surface diffusion model, or (▬ ▬) parallel pore and surface diffusion model ($D_p = 1.5 \times 10^{-6}$ and $D_s = 1.7 \times 10^{-7}$ cm^2/min, unless noted otherwise).

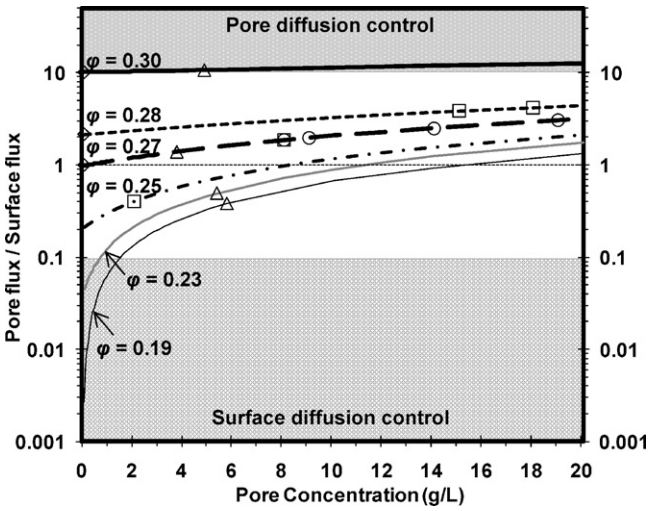

Fig. 6. . The ratio of pore diffusion flux to surface diffusion flux as a function of φ and pore concentration. A parallel pore and surface diffusion model can be used to predict the breakthrough curve and elution profiles, when the ratio is close to 1. (◊) isocratic pulse, (△) frontal, (□) stepwise elution, and (○) linear gradient elution runs.

rities and LPI were similar, the mass transfer parameters of the impurities were assumed to be the same as those of LPI. Most of the mass transfer parameters, except pore diffusivity and surface diffusivity, were estimated from literature correlations. The axial dispersion coefficient, E_b, was calculated using the Chung and Wen correlation unless noted otherwise [62]. The Brownian diffusivity, D_∞, of lispro insulin in a solution of 5 g/L at pH 7.8 was 5.22×10^{-5} cm^2/min between 14 and 17 °C [63]. The Brownian diffusivity of MeCN was 7.31×10^{-4} cm^2/min at 15 °C [64]. The film mass transfer coefficient, k_f, was estimated using the Wilson and Geankoplis correlation [65].

The strategy discussed in Section 2.4 was applied to estimate intrinsic pore diffusivity and surface diffusivity of LPI. The intrinsic pore diffusivity, D_p, was estimated by comparing simulations with the elution profile of a small pulse at $\varphi = 0.60$ (Fig. 3a). The D_p estimated was 1.5×10^{-6} cm^2/min. The apparent pore diffusivity, $D_{p,app}$, at $\varphi = 0.27$ was estimated to be 2.7×10^{-6} cm^2/min by comparing simulations based on the pore diffusion model with the low concentration portion of the breakthrough curve (Fig. 5b). The $D_{p,app}$ was larger than the intrinsic D_p estimated from the isocratic pulse at $\varphi = 0.6$, indicating that both pore diffusion and surface diffusion contribute to intraparticle diffusion. The D_s of LPI was then estimated from the D_p and Eq. (21a) to be 1.7×10^{-7} cm^2/min. Table 5 summarizes the mass transfer parameters used in the simulations in this study.

4.6.2. Ratio of pore diffusion flux to surface diffusion flux, $D_{p,app}$ and $D_{s,app}$ as a function of φ and C_p

If the isotherm parameters, D_p and D_s are known, one can use Eq. (22d) and plot the ratio of pore diffusion flux to surface diffusion flux as a function of φ and C_p (Fig. 6). When $\varphi \geq 0.30$ ($a(\varphi) < 0.4$), as expected from Eq. (23a), the flux ratio is greater than 10 for all concentrations, and this is defined as the pore diffusion control region (Fig. 6). Similarly, the region with a flux ratio less than 0.1 is defined as the surface diffusion control region. The region with a flux ratio between 0.1 and 10 is defined as the parallel diffusion region.

Notice that most of the experimental data are in the parallel diffusion region, except the low concentration portions ($C_p < 1$ g/L) of the frontals at $\varphi = 0.23$ and 0.19, which are in the surface diffusion control region. Specifically, all the linear gradient elution runs and stepwise elution runs (except the first elution step in S3) have a ratio of pore diffusion flux to surface diffusion flux between 1 and 4. The high concentration portions of the frontals at $\varphi = 0.19$ and 0.23 and the first elution step in S3 ($\varphi = 0.25$) have a ratio of surface diffusion flux to pore diffusion flux between 3 and 5.

If D_p and D_s are constant, one can calculate and plot $D_{p,app}$ (if estimated using the pore diffusion model) and $D_{s,app}$ (if estimated using the surface diffusion model) as a function of φ and C_p (Fig. 7). The $D_{p,app}$ (solid line) and $D_{s,app}$ (dashed line) can vary by several orders of magnitude, because the concentration gradients in the pore phase and on the surface depend strongly on φ and C_p. The surface concentration can vary with φ by three orders of magnitude. The pore phase concentration can also vary by five orders of magnitude depending on the loading volume (from 0.0004 CV pulse to 13 CV frontal). The results in Fig. 7 suggest that for a parallel pore and surface diffusion system, neither a pore diffusion model nor a surface diffusion model can use a constant diffusivity to predict the frontal and elution profiles over the wide range of φ's and C_p's. The predictions in Fig. 7 are first discussed below and then compared with the apparent diffusivities ($D_{p,app}$ and $D_{s,app}$) estimated from all the runs.

At $\varphi = 0.3$, since little LPI is adsorbed ($a = 0.4$ and $b = 0.01$ L/g), pore diffusion dominates at all concentrations (Fig. 6). $D_{p,app}$ (solid line in Fig. 7a) is almost the same as D_p, and it is independent of concentration, because contribution from surface diffusion is negligible. $D_{s,app}$ (dashed line in Fig. 7a) is slightly greater than D_p, because $\varepsilon_p(1-\varepsilon_b)/a(\varphi)$ in Eq. (21b) is greater than 1. The predic-

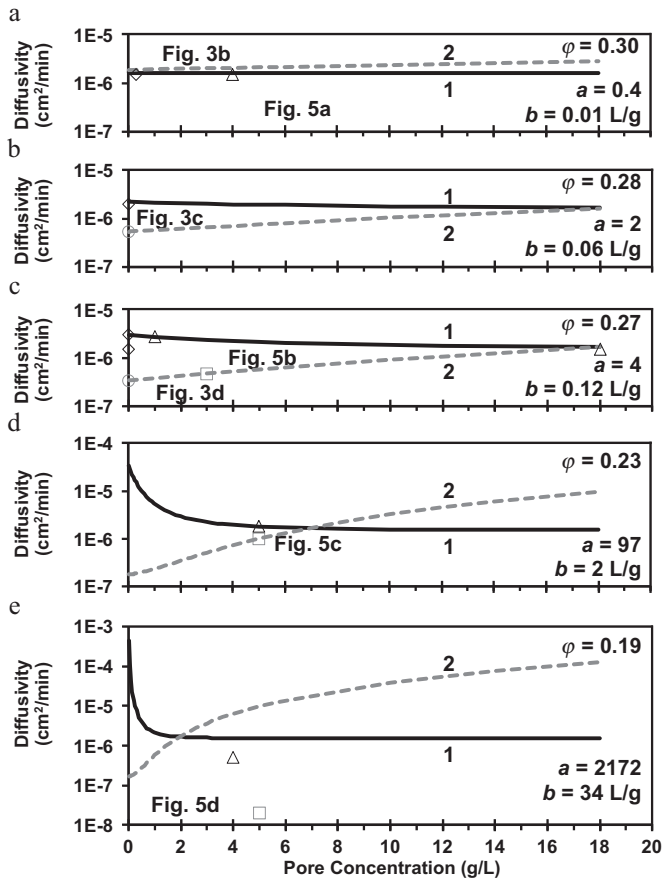

Fig. 7. The apparent pore diffusivity and apparent surface diffusivity as a function of φ and pore concentration. Lines are model predictions and symbols are experimental data. (◊) is $D_{p,app}$ estimated from isocratic pulse, (△) is $D_{p,app}$ estimated from breakthrough curve, (○) is $D_{s,app}$ estimated from isocratic pulse, and (□) is $D_{s,app}$ estimated from breakthrough curve. The model is based on $D_p = 1.5 \times 10^{-6}$ cm^2/min and $D_s = 1.7 \times 10^{-7}$ cm^2/min. Curve 1 is $D_{p,app}$ (Eq. (21a)); curve 2 is $D_{s,app}$ (Eq. (21b)).

tions in Fig. 7 indicate that for $\varphi \geq 0.3$, a pore diffusion model with a constant D_p can model a parallel pore and surface diffusion system. A surface diffusion model can also work in this φ range. However, the $D_{s,app}$ is an order of magnitude higher than the intrinsic D_s, and $D_{s,app}$ can increase slightly with increasing concentration (Fig. 7a).

At $\varphi < 0.3$, $D_{p,app}$ (solid line) and $D_{s,app}$ (dashed line) strongly depend on φ and C_p (Fig. 7b–e). As expected from Eq. (21a), at a low concentration, $D_{p,app}$ is greater than D_p, because of significant contributions from surface diffusion (Fig. 7b–e). As concentration increases, the contribution from surface diffusion is diminished, $D_{p,app}$ approaches D_p at high pore concentrations.

The contribution from pore diffusion is negligible at a low pore concentration and a low φ. For this reason, the $D_{s,app}$ (dashed lines in Fig. 7b–e) approaches D_s for $\varphi < 0.3$. As concentration increases, pore diffusion contribution becomes increasingly more important, as expected from Eq. (21a). The estimated $D_{s,app}$ can be much larger than D_s, and is expected to increase with increasing concentration (Fig. 7b–e).

Experimental $D_{p,app}$ (diamonds estimated from pulse data and triangles from frontals) and $D_{s,app}$ (circles from pulse data and squares from frontals) are compared with the predicted $D_{p,app}$ (solid lines) and $D_{s,app}$ (dashed lines) in Fig. 7. At $\varphi = 0.3$, the $D_{p,app}$ values estimated from the breakthrough curve (Fig. 5a) and from the adsorption wave of the small pulse in isocratic elution (Fig. 3b) agree with the predictions of the parallel diffusion model (solid line in Fig. 7a).

At $\varphi = 0.27$ and 0.28, $D_{p,app}$ (diamonds) and $D_{s,app}$ (circles) estimated from the adsorption wave of the small pulse in isocratic elution (Fig. 3c and d) agree with the prediction of the parallel diffusion model in Fig. 7b and c. The $D_{p,app}$ was larger than D_p, because of the contribution of surface diffusion. Since the contribution from surface diffusion decreases with increasing concentration, the $D_{p,app}$ estimated from the breakthrough curve at 18 g/L (frontal data not shown) is close to D_p (Fig. 7c). This result also agrees with the prediction of the parallel diffusion model.

When φ was 0.23 or smaller, retention time in isocratic elution was too long to allow detection of a small pulse. Therefore, only the diffusivities estimated from the breakthrough curves could be compared with the predictions. At $\varphi = 0.23$, the $D_{p,app}$ (triangle) and $D_{s,app}$ (square) estimated from the breakthrough curve (Fig. 5c) agree with the predictions of the parallel diffusion model in Fig. 7d. At this feed concentration, 5.3 g/L, $a(\varphi) = 97.4$ and $b(\varphi)C_p = 10$, $D_{s,app}$ and $D_{p,app}$ values are similar as expected from Eq. (21).

All the pulse and frontal data are consistent with the parallel diffusion model with $D_p = 1.5 \times 10^{-6}$ and $D_s = 1.7 \times 10^{-7}$ cm^2/min. The high concentration portion of the frontal data (>3 g/L) at $\varphi = 0.19$ is the only exception. At $\varphi = 0.19$, $D_{p,app}$ predicted should approach D_p ($D_{p,app} = D_p + 0.11D_s$) and a high $D_{s,app}$, $\sim 9D_p$ ($D_{s,app} = D_s + 9D_p$) was predicted for the frontal at 5.7 g/L (Fig. 7e). As such, the parallel diffusion model predicts a relatively sharp breakthrough curve for F4 (Fig. 5d). However, the experimental breakthrough curve at the high concentration region shows slow approach to saturation, which is a characteristic for surface diffusion, and cannot be predicted closely by a pore diffusion model with any D_p value (see Supplementary Fig. Bb). F4 also cannot be predicted by the surface diffusion model with a constant $D_{s,app}$. The low concentration portion of the breakthrough curve (<3 g/L) can be explained using $D_{s,app}$ $\sim 5 \times 10^{-8}$ cm^2/min, whereas the high concentration portion using $D_{s,app}$ about 10^{-8} cm^2/min (Supplementary Fig. Bc). The $D_{s,app}$ estimated does not increase with increasing concentration as expected from Eq. (21b). On the contrary, the $D_{s,app}$ estimated decreases with increasing concentration (Supplementary Fig. Bc). The high concentration portion of the breakthrough curve (F4) can be predicted closely using a parallel diffusion model if the intrinsic diffusivities are reduced by an order of magnitude, $D_p = D_s = 10^{-8}$ cm^2/min. The surface diffusivity could be reduced because the concentration of LPI adsorbed on the sorbent surface at $\varphi = 0.19$ reached q_{max} (64 g/L CV) at a pore concentration of 3 g/L (Fig. 4c). Since the C8 sorbent has an average pore diameter of 100 Å, the diffusivity of LPI (20 Å × 25 Å × 30 Å) in the pores can also be hindered and reduced by the adsorbed LPI in the high concentration region (>3 g/L).

4.7. Model verification with elution profiles

4.7.1. Model verification with pulse profiles

To verify the rate model and model parameters, VERSE simulations with the estimated parameters are compared with linear gradient (Fig. 2) and isocratic pulse profiles (Fig. 3). The retention time of the peaks can be predicted closely by the rate model, as discussed in Section 4.4.2. At $\varphi = 0.6$, LPI adsorption is negligible and the experimental pulse is slightly more asymmetric than predicted (Fig. 3a). The discrepancy can be due to slightly nonuniform packing or a small amount of dead volume within the column [66].

As φ decreases, the isocratic elution peaks show more pronounced tailing (Fig. 3b–d). The asymmetric peaks cannot be due to nonlinear effects, since the pulse size is small (100 μL) and $bC_p \ll 1$. Furthermore, the peak tailing was reduced as the pulse size increased from 5 (0.0004 CV) to 100 μL (0.01 CV) (results not shown). Such tailing could not be attributed to mixing in the extra column dead volume, since the simulations already took into account extra-column mixing by the two CSTR's. The effect of MeCN adsorption was also ruled out as a cause for peak tailing, since sym-

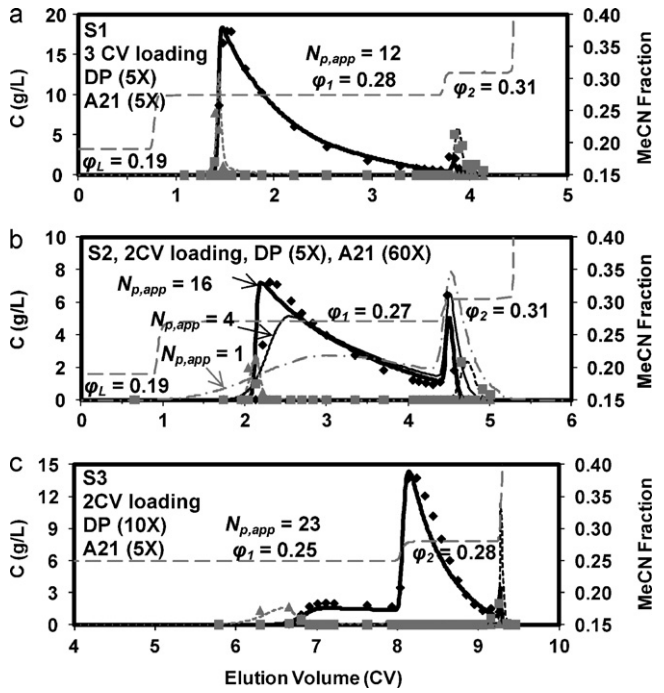

Fig. 8. Verification of the rate model and the model parameters with the large loading stepwise elution runs: (a) S1, (b) S2, and (c) S3. Symbols are HPLC results: (▲) DP, (♦) LPI, and (■) A21; lines are model predictions based on parameters in Table 5: (▬ ▬) MeCN fraction at column outlet; (■ ■ ■ ■ ■) DP, (▬) LPI, and (.....) A21. Others are noted in the figure.

metric LPI peaks were predicted when the adsorption isotherm of MeCN was included in the simulation.

The tailing in the linear region (≤0.01 CV loading) could be attributed to the heterogeneous C8 stationary phase. Proteins, LPI for example, could interact more strongly with a small amount of high energy sites [67]. The high affinity sites could result in peak tailing at low loading (<0.01 CV). A dual-site Langmuir isotherm can be used in the rate model to simulate such tailing [42]. Moreover, a non-spherical solute can adsorb on the stationary phase with mostly side-on orientation at a low coverage and end-on orientation at a high coverage. The solutes with the side-on orientation can adsorb more strongly with the stationary phase, resulting in the peak tailing in the linear region [68]. However, peak tailing due to heterogeneity in binding sites or binding orientation at the low loading (<0.01 CV) is apparently negligible at high loading (≥2 CV) as shown in the chromatograms of stepwise and linear gradient elution runs in the section below.

4.7.2. Model verification with large loading stepwise elution and linear gradient elution profiles

VERSE simulations with estimated parameters are compared with the large loading (≥2 CV loading) stepwise elution and linear gradient elution profiles (Figs. 8 and 9). In these runs, LPI and impurities were eluted when $\varphi \geq 0.27$, except the first elution step in S3. The contributions from surface diffusion are expected to result in a $D_{p,app}$ which is 30–50% greater than D_p as expected from Fig. 7a–c. However, the waves are sharp in this velocity range because of the small particle size and furthermore, the waves are sharpened by the gradient. The small increase in $D_{p,app}$ does not have discernable effect on the peak shapes (more discussion can be found in the sensitivity studies in Section 4.7.4). As a result, a pore diffusion model with a constant D_p can predict closely the peak shapes of LPI and DP in the large loading stepwise and linear gradient elution runs (Figs. 8 and 9). The adsorption and desorption waves for all the runs at an interstitial velocity less than 10 cm/min

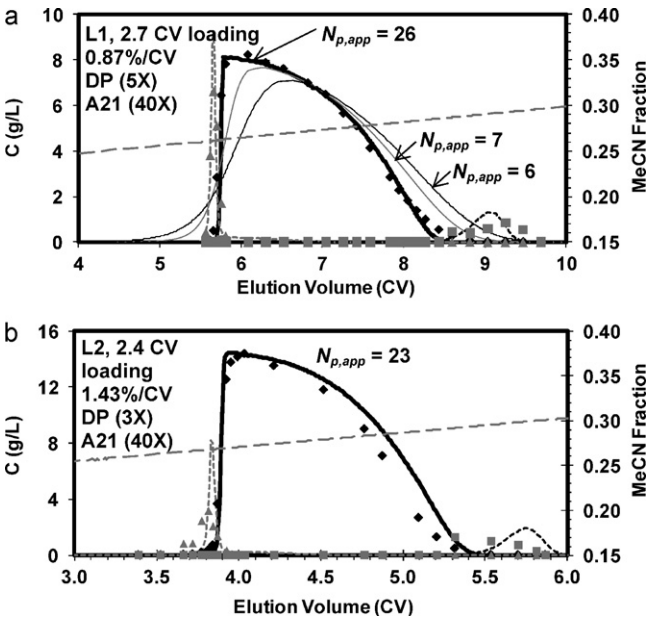

Fig. 9. Verification of the rate model and the model parameters with the large loading linear gradient elution runs: (a) L1 and (b) L2. Symbols are HPLC results: (▲) DP, (♦) LPI, and (■) A21; lines are model predictions based on parameters in Table 5: (▬ ▬) MeCN fraction at column outlet; (■ ■ ■ ■ ■) DP, (▬) LPI, and (.....) A21. Others are noted in the figure.

are predicted within experimental errors (±3%) for LPI and the impurities.

4.7.3. Peak tailing at a high loading (>4 CV) and a high elution velocity (u_0 > 10 cm/min)

Among the large loading linear gradient elution runs, long tailing was observed in L3 and L4 (Fig. 10). One possible reason for the peak tailing is viscous fingering at a high elution velocity (u_0 = 11.3 cm/min) for the high loading (>4 CV). The elution velocities in L3 and L4 were about three times of those in L1 and L2. When a more viscous protein solution was dis-

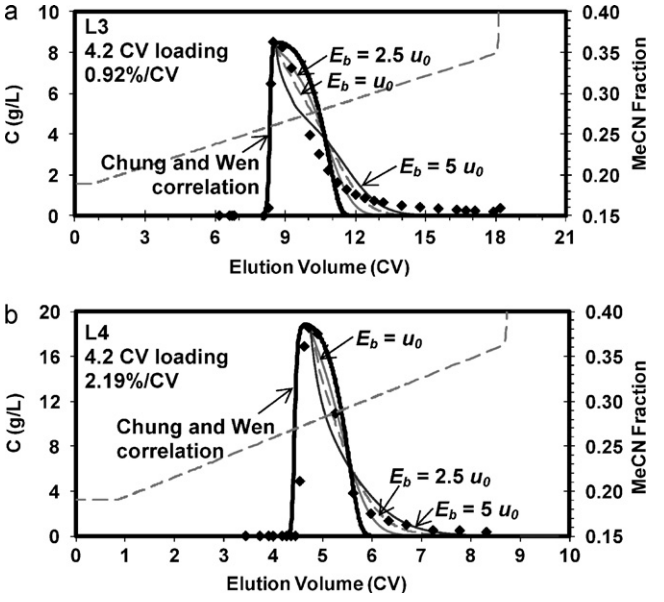

Fig. 10. Verification of the rate model and the model parameters with the large loading linear gradient elution run: (a) L3 and (b) L4. (♦) HPLC results of LPI; lines are model predictions: (▬ ▬) MeCN fraction at column outlet; (▬) LPI, local equilibrium, Chung and Wen correlation. Others are noted in the figure.

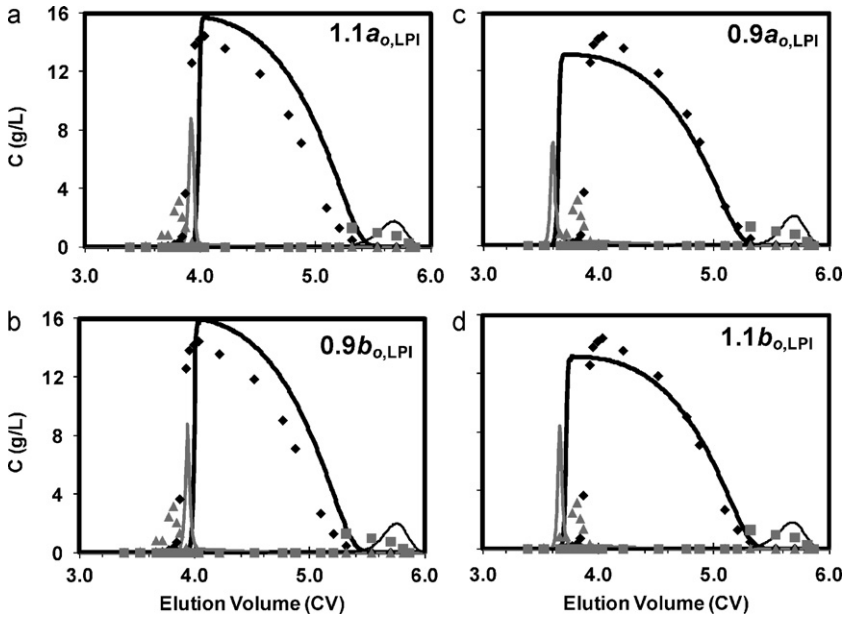

Fig. 11. Sensitivity of elution profiles to isotherm parameters of LPI. Symbols are HPLC results from L2: (▲) 3X DP, (♦) LPI, and (■) 40X A21; lines are model predictions: (▬) DP, (▬) LPI, and (▬) A21. Simulations are based on parameters in Table 5 with the following changes in isotherm parameters: (a) 1.1$a_{o,LPI}$, (b) 0.9$b_{o,LPI}$, (c) 0.9$a_{o,LPI}$, and (d) 1.1$b_{o,LPI}$.

placed by a less viscous mobile phase (acetonitrile in morpholine buffer), the interface became unstable. Instead of a plug flow profile at the interface, the low viscosity mobile phase forms fingers into the more viscous protein band. To simulate such phenomenon, the axial dispersion coefficient during elution was correlated using an empirical correlation (E_b is linearly proportional to u_0). Simulations using the correlation show better agreement with the experimental data in L3 and L4 (Fig. 10). The results indicate that the tailing could be caused by viscous fingering at a high loading and a high elution velocity ($u_0 > 10$ cm/min). A similar correlation was tested successfully to take into account dispersion due to viscous fingering in previous studies of sugar solutions [19,20].

4.7.4. Effect of gradient focusing on peak shape in stepwise and linear gradient elution

Simulations were carried out for the three large loading stepwise elution runs (Fig. 8). In S1, most of the LPI eluted in the first elution step (Fig. 8a). In S2 and S3, some LPI eluted in the first step and the remaining solute was focused and eluted in the second elution and the regeneration steps (Fig. 8b and c).

The LPI adsorption wave for S1 during loading ($\varphi = 0.19$) was self-sharpening because of the high affinity during loading ($a = 2172$ and $b = 34$ L/g). When a step change in $\varphi = 0.28$ was introduced in the first elution step, the adsorption wave was also focused by the step increase in φ. The adsorption wave in S2 (Fig. 8b) was less sharp than that in S1 (Fig. 8a), because φ in the first elution step ($\varphi_1 = 0.27$) in S2 was lower than φ_1 in S1 (=0.28). As a result, the adsorption wave in S2 was less focused by the smaller step change in φ. For a similar reason, the adsorption wave in S3 ($\varphi_1 = 0.25$, Fig. 8c) was less sharp than in S2. During the elution steps, the desorption waves in all three cases were broadened by nonlinear effects.

Simulations were carried out for the large loading linear gradient elution runs (Fig. 9). Similar to stepwise elution runs, the adsorption waves during loading ($\varphi = 0.19$) were self-sharpening. The adsorption waves were further focused by the increasing φ during elution. The maximum concentration for the adsorption wave was lower in L1 (Fig. 9a) than that in L2 (Fig. 9b), because the gradient slope in L1 (0.87%/CV) was smaller than in L2 (1.43%/CV). For the same reason, the peak width in L1 (3 CV) was wider than that in L2 (1.5 CV).

If the estimated $a_{o,LPI}$ or $b_{o,LPI}$ is off by 10%, the predicted elution profiles of LPI are affected significantly (Fig. 11). When $a_{o,LPI}$ is increased by 10% or $b_{o,LPI}$ is decreased by 10%, the capacity of LPI during loading ($q_{o,LPI}$) is increased by 10%, resulting in a more focused LPI peak with a longer retention time (Fig. 11a and b). A decrease in $a_{o,LPI}$ or an increase in $b_{o,LPI}$ by 10% results in a broader LPI peak with a shorter retention time (Fig. 11c and d). More importantly, since the low affinity impurity DP is displaced by LPI, the elution time of DP is controlled by the adsorption wave of LPI. The errors in LPI isotherm parameters affect significantly the predicted elution profiles of DP. By contrast, the elution profiles of the high affinity impurity A21 are slightly affected by the errors in LPI isotherms. The eluted peak width of DP is less than 0.2 CV, which is less than 5% of the net elution time of the LPI adsorption wave. The separation of DP from LPI cannot be predicted if the LPI isotherm parameters have 10% errors (Fig. 11). The experimental and the predicted yield values for the specified product purity requirements are compared for stepwise elution runs and linear gradient runs in Tables 3 and 4. The accuracy of the experimental yield values is slightly lower than predicted, because the size of the fraction collected at the column effluent for HPLC analysis was limited to 1 mL. In the simulation, the product peak can be cut precisely according to the purity requirement. The differences between the predicted and the experimental yield values are less than 2%. The close agreement indicates that the estimated isotherm parameters are quite accurate.

4.7.5. Effect of diffusion on peak shape in stepwise and linear gradient elution

While gradient focusing sharpens the waves, diffusion broadens the waves during peak migration. A key dimensionless group, N_p ($=\varepsilon_p D_p L/u_0 R^2$) which is a characteristic diffusion rate relative to a characteristic convection rate, allows us to compare the diffusion effects at different velocities in these runs. Since all these runs are in the parallel diffusion region, $D_{p,app}(\varphi, C_p)$ instead of the intrinsic D_p is used in calculating $N_{p,app}$. The values are listed in Tables 3 and 4.

In the two stepwise elution runs (S1 and S2) and the two linear gradient elution runs (L1 and L2), the LPI peaks are eluted at $\varphi \geq 0.27$ (Figs. 8a, b, and 9). For these cases, the $N_{p,app}$ values are greater than 10. Further increase in $N_{p,app}$ in simulations has no effect on the predicted profiles. Apparently, when $N_{p,app} \geq 10$, the focusing effects for loading at $\varphi = 0.19$ and elution at $\varphi \geq 0.27$ are sufficiently strong to overcome the relatively small diffusion spreading. As $N_{p,app}$ is reduced to less than 10 by increasing particle size or increasing velocity, the wave broadening due to diffusion cannot be completely compensated by the focusing effects (Figs. 8b and 9a).

In S3, in spite of the high $N_{p,app}$ (=23) during the first elution step at $\varphi = 0.25$, the LPI adsorption wave was broadened by diffusion (Fig. 8c). Apparently, the focusing effects for loading at $\varphi = 0.19$ and elution at $\varphi = 0.25$ are weaker than all the other runs where elution occurs at $\varphi \geq 0.27$.

5. Conclusions

The adsorbed LPI can be recovered with high purity (≥99.5%) and high yield (≥95%) using stepwise and linear gradient elution in RPC under the conditions tested (Tables 3 and 4). Since the diffusion rates are slow compared to adsorption and desorption rates (Supplementary Table C), one can use equilibrium isotherms in the rate model to describe the adsorption and desorption of LPI and impurities.

The isotherms of LPI and impurities can be described by a modified reversed phase modulator isotherm. The solvent-modulated isotherm parameters account for the effects of MeCN adsorption and the modulation of LPI adsorption by MeCN. Although LPI has an intrinsic size exclusion factor of 0.75, the effects of size exclusion are minor and can be taken into account by the isotherm modulation parameters when φ is between 0.19 and 0.40 (Supplementary Fig. A).

An efficient method has been developed for estimating isotherm parameters over a wide range of φ's. The linear isotherm parameters are estimated from the retention times of two or more pulse linear gradient elution runs at different gradient slopes. The nonlinear isotherm parameters are estimated from frontal data at three or more φs. Compared to frontal analysis, this method requires less material and an order of magnitude fewer experiments.

In this study, we have developed a parallel pore and surface diffusion model for LPI and the impurities because preliminary studies showed that the asymmetric breakthrough curves of LPI at a low φ could not be explained by a pore diffusion model. Furthermore, the $D_{p,app}$ estimated from a pore diffusion model and the $D_{s,app}$ estimated from a surface diffusion model varied significantly with LPI concentration and φ. We develop a strategy to estimate the intrinsic diffusivities. The intrinsic D_p is estimated from pulse data at a high φ ($\varphi \geq 0.6$), where protein adsorption is negligible. $D_{p,app}$ and $D_{s,app}$ are estimated from the frontal data in a parallel diffusion region, where the contributions from pore diffusion and from surface diffusion are comparable. The intrinsic diffusivities allow us to identify the φ and pore concentration regions where (1) pore diffusion flux dominates, (2) surface diffusion flux dominates, or (3) pore and surface diffusion fluxes are comparable.

The results show that the parallel pore and surface diffusion model with constant intrinsic diffusivities (D_p and D_s) can predict most of the breakthrough curves and elution profiles over a wide range of φ's (0.19–0.40), concentrations (0.05–18 g/L), loading volume (0.0004–13 CV), and interstitial velocities ($u_0 < 10$ cm/min) (Figs. 2, 3, 5, 8, and 9). For a small pulse (0.0004–0.01 CV) in isocratic or gradient elution, the retention times are well predicted, but not peak tailing, which could be due to the presence of a small amount of high energy adsorption sites in the sorbent or heterogeneity in adsorption orientation. The high concentration portion (>3 g/L) of the frontal data at $\varphi = 0.19$ can be predicted closely if both D_p and D_s are reduced at the high surface concentration (64 g/L) (Fig. 5d).

The linear isotherm parameters of LPI and the impurities decrease by four orders of magnitudes as φ increases from 0.19 to 0.40. As a result, the ratio of pore diffusion flux to surface diffusion flux, $D_{p,app}$ (estimated from a pore diffusion model) or $D_{s,app}$ (estimated from a surface diffusion model) can also vary by several orders of magnitude depending on φ and C_p (Fig. 7). In the surface diffusion dominating or parallel diffusion regions, breakthrough curves at a high concentration can be asymmetric because surface concentration gradient diminishes as the surface approaches saturation.

Contributions from surface diffusion can also cause an apparent increase in $D_{p,app}$ for a small pulse (≤0.01 CV loading) at $\varphi \leq 0.28$. At a low $\varphi \leq 0.23$, the surface concentration gradient can be much larger than that in the pore phase. Since $D_{p,app}$ is estimated based on the pore concentration gradient without considering the surface flux, the $D_{p,app}$ estimated can be greater than the intrinsic D_p. As C_p increases as loading volume increases or solvent strength decreases in gradient elution, the pore diffusion flux can be much greater than the surface diffusion flux. The $D_{p,app}$ estimated from the pore diffusion model can approach the intrinsic D_p. The $D_{s,app}$ estimated in the parallel diffusion region approaches the intrinsic D_s at a very low C_p and always increases with increasing C_p because of increasing contribution from pore diffusion.

In the parallel diffusion region, where the ratio of pore diffusion flux is greater than surface diffusion flux, a pore diffusion model with a constant $D_{p,app}$ or a surface diffusion model with a constant $D_{s,app}$ cannot predict closely the isocratic elution profiles of the small pulses when φ varies from 0.27 to 0.30 (Fig. 3b–d). When surface diffusion flux to pore diffusion flux is much greater than 1 in the parallel diffusion region, the contribution from surface diffusion are significant. A pore diffusion model cannot predict closely the asymmetric breakthrough curves at $\varphi \leq 0.23$. A surface diffusion model or a parallel diffusion model can predict closely the frontal profiles (Fig. 5c).

In stepwise and linear gradient elution at a high loading (2–3 CV), LPI and impurities are loaded at a low φ (0.19) and eluted in a region of relatively high φ (0.27 or higher). The elution peaks are strongly sharpened and focused by the gradient because of the large affinity difference between the loading φ and the elution φ. When $N_{p,app} \geq 10$, the diffusion spreading is mostly compensated by the gradient focusing. Although $D_{p,app}$ is 2 or 3 times of the intrinsic D_p, contributions from surface diffusion during elution do not have discernable effects on the focused peaks because of the strong focusing effect and the high $N_{p,app}$. For this reason, a pore diffusion model with a constant $D_{p,app}$ can predict closely the elution profiles of LPI and the impurities for stepwise and linear gradient elution (Figs. 8 and 9). The experimental yield values (≥95%) are predicted to within ±1% by the model.

Nomenclature

a	linear isotherm parameter at an effective organic fraction
a_o	linear isotherm parameter at the reference organic fraction
b	nonlinear isotherm parameter at an effective organic fraction
$B_{f,i}$	film mass transfer rate/axial convection rate for species i ($=k_{f,i}L/u_0R$)
Bi_i	Biot number for species i ($=k_{f,i}R/\varepsilon_p D_{p,i}$)

b_o nonlinear isotherm parameter at the reference organic fraction
C concentration of the solute
C_e maximal possible inlet concentration or a reference concentration
c_i dimensionless concentration for species i
CV column volume
D_∞ Brownian diffusivity
D_p intrinsic pore diffusivity
D_s intrinsic surface diffusivity
DV dead volume of the system
E_b axial dispersion coefficient
k capacity factor
Ke size exclusion factor
k_f film mass transfer coefficient
k_o capacity factor at the reference organic fraction
$l_{o,-}$ reaction rate constant of desorption
$l_{o,+}$ reaction rate constant of adsorption
MeCN acetonitrile
$N_{f,i}$ film mass transfer rate/axial convection rate for species i ($=3L(1-\varepsilon_b)k_{f,i}/R\varepsilon_b u_0$)
$N_{l-,i}$ desorption rate/axial convection rate for species i ($=Ll_{-,i}(\varphi_e)/u_0$)
$N_{l+,i}$ adsorption rate/axial convection rate for species i ($=Ll_{+,i}(\varphi_e)C_{e,i}/u_0$)
$N_{p,i}$ intraparticle diffusion rate/axial convection rate for species i ($=\varepsilon_p LD_{p,i}/u_0R^2$)
$N_{s,i}$ surface diffusion rate/axial convection rate for species i ($=LD_{s,i}/u_0R^2$)
$Pe_{b,i}$ axial Peclet number for species i ($=u_0L/E_{b,i}$)
q amount of solute adsorbed per column volume
q_{max} the maximum capacity of the column ($=q_{max}(\varphi)=a(\varphi)/b(\varphi)$)
r particle position
R particle radius
S slope of $\log_{10} k$ versus φ
S_- desorption kinetic parameter
S_+ adsorption kinetic parameter
S_a linear isotherm parameter
S_b nonlinear isotherm parameter
t_{br} mass center time or retention time of the breakthrough curve
t_d dwell time
TG gradient time, time for φ varying from φ_0 to φ_f
t_{GR} solute retention time in linear gradient elution run
t_r retention time in isocratic elution (Eq. (10a))
u_0 interstitial velocity
V_{br} breakthrough volume in frontal experiments
x dimensionless axial column position ($=z/L$)
$Y_{l,i}$ net adsorption rate
z axial column position

Greek letters

ϕ_L loading factor $=C_{e,i}/[(1-\varepsilon_p)\bar{C}_{T,i}]$
ε_b interparticle voidage
ε_p intraparticle voidage
ε_t total voidage
θ dimensionless time ($=t/\tau$)
ξ dimensionless particle position ($=r/R$)
τ percolation time ($=L/u_0$)
φ organic fraction, acetonitrile fraction in this study
φ_0 initial organic fraction in a linear gradient elution process
φ_1 organic fraction of the first elution step
φ_2 organic fraction of the second elution step
φ_e effective $\varphi=\varphi-0.19$
φ_f final organic fraction in a linear gradient elution process

Subscripts

app apparent
b bulk phase
f feed solution
i, j component counters
n property in the *n*-th run
new property of a fresh or new column
old property of an older column
p particle phase
s surface
T maximum capacity per solid volume

Diacritic

$\bar{}$ solid phase

Acknowledgments

We are grateful to Eli Lilly & Co. for supporting this study. We thank Dr. Francis Dwulet, Mr. David Hoggatt, Ms. Sarah James, Dr. Frederick Larimore, Dr. Warren MacKellar, Dr. James McDonough, Dr. Andrew Russell, Dr. Graham Tulloch, and Dr. Terri Vicenizi for their advice, help, and support.

Appendix A. Supplementary data

Supplementary data associated with this article can be found, in the online version, at doi:10.1016/j.chroma.2010.09.078.

References

[1] D. Petrides, E. Sapidou, J. Calandranis, Biotechnol. Bioeng. 48 (1995) 529.
[2] F. Holleman, J.B.L. Hoekstra, N. Engl. J. Med. 337 (1997) 176.
[3] J.H. Anderson, R.E. Chance, R.D. DiMarchi, B.H. Frank, Abstr. Pap. Am. Chem. Soc. 215 (1998) U892.
[4] G. Schernthaner, W. Wein, K. Sandholzer, S. Equiluz-Bruck, P.C. Bates, M.A. Birkett, Diabetes Care 21 (1998) 570.
[5] Z. Vajo, J. Fawcett, W.C. Duckworth, Endocr. Rev. 22 (2001) 706.
[6] J.D. Meece, R.K. Campbell, Diabetes Educ. 28 (2002) 269.
[7] D.N. Brems, P.L. Brown, C. Bryant, R.E. Chance, R.D. Dimarchi, L.K. Green, D.C. Howey, H.B. Long, A.A. Miller, R. Millican, A.H. Pekar, J.E. Shields, B.H. Frank, ACS Symp. Ser. 526 (1993) 254.
[8] R.E. Chance, B.H. Frank, J.M. Radziuk, R.D. DiMarchi, Drugs Today 34 (1998) 1.
[9] F.G. Hamel, G.L. Siford, J. Fawcett, R.E. Chance, B.H. Frank, W.C. Duckworth, Metabolism 48 (1999) 611.
[10] E.P. Kroeff, R.A. Owens, E.L. Campbell, R.D. Johnson, H.I. Marks, J. Chromatogr. 461 (1989) 45.
[11] X.D. Liu, K. Kaczmarski, A. Cavazzini, P. Szabelski, D.M. Zhou, G. Guiochon, Biotechnol. Prog. 18 (2002) 796.
[12] M. Gubernak, X.D. Liu, K. Kaczmarski, G. Guiochon, Biotechnol. Prog. 20 (2004) 1496.
[13] M. Degerman, N. Jakobsson, B. Nilsson, J. Chromatogr. A 1162 (2007) 41.
[14] Z. Ma, R.D. Whitley, N.-H.L. Wang, AIChE J. 42 (1996) 1244.
[15] A.P. Sabharwal, H.A. Chase, Food Bioprod. Process 77 (1999) 18.
[16] X.D. Geng, F.E. Regnier, Chin. J. Chem. 21 (2003) 429.
[17] Y. Zhou, M. Ottens, E. Hansen, L.A.M. van der Wielen, J. Chromatogr. A 1061 (2004) 141.
[18] J.A. Berninger, R.D. Whitley, X. Zhang, N.-H.L. Wang, Comput. Chem. Eng. 15 (1991) 749.
[19] R.D. Whitley, J.A. Berninger, N. Rouhana, N.-H.L. Wang, Biotechnol. Prog. 7 (1991) 544.
[20] R.D. Whitley, K.E. Van Cott, J.A. Berninger, N.-H.L. Wang, AIChE J. 37 (1991) 555.
[21] K.E. Van Cott, R.D. Whitley, N.-H.L. Wang, Sep. Technol. 1 (1991) 142.
[22] S.U. Kim, J.A. Berninger, Q. Yu, N.-H.L. Wang, Ind. Eng. Chem. Res. 31 (1992) 1717.
[23] R.D. Whitley, K.E. Van Cott, N.-H.L. Wang, Ind. Eng. Chem. Res. 32 (1993) 149.
[24] R.D. Whitley, X. Zhang, N.-H.L. Wang, AIChE J. 40 (1994) 1067.
[25] Z. Ma, D. Tanzil, B.W. Au, N.-H.L. Wang, Biotechnol. Prog. 12 (1996) 810.
[26] M.V. Ernest, R.D. Whitley, Z. Ma, N.-H.L. Wang, Ind. Eng. Chem. Res. 36 (1997) 212.
[27] M.V. Ernest, J.P. Bibler, R.D. Whitley, N.-H.L. Wang, Ind. Eng. Chem. Res. 36 (1997) 2775.
[28] B.J. Hritzko, M.J. Ortiz-Vega, N.-H.L. Wang, Ind. Eng. Chem. Res. 38 (1999) 2754.
[29] Y. Xie, E. Van de Sandt, T. de Weerd, N.-H.L. Wang, J. Chromatogr. A 908 (2001) 273.
[30] Y. Xie, D. Phelps, C.H. Lee, M. Sedlak, N. Ho, N.-H.L. Wang, Ind. Eng. Chem. Res. 44 (2005) 6816.
[31] C.-M. Yu, S. Mun, N.-H.L. Wang, J. Chromatogr. A 1192 (2008) 121.

[32] S. Mun, N.-H.L. Wang, Ind. Eng. Chem. Res. 45 (2006) 1058.
[33] R. Wooley, Z. Ma, N.-H.L. Wang, Ind. Eng. Chem. Res. 37 (1998) 3699.
[34] Y. Xie, D. Wu, Z. Ma, N.-H.L. Wang, Ind. Eng. Chem. Res. 39 (2000) 1993.
[35] B.J. Hritzko, Y. Xie, R.J. Wooley, N.-H.L. Wang, AIChE J. 48 (2002) 2769.
[36] S.Y. Mun, Y. Xie, J.H. Kim, N.-H.L. Wang, Ind. Eng. Chem. Res. 42 (2003) 1977.
[37] S.Y. Mun, Y. Xie, N.-H.L. Wang, AIChE J. 49 (2003) 2039.
[38] S. Mun, Y. Xie, N.-H.L. Wang, Ind. Eng. Chem. Res. 42 (2003) 3129.
[39] Y. Xie, B. Hritzko, C.Y. Chin, N.-H.L. Wang, Ind. Eng. Chem. Res. 42 (2003) 4055.
[40] Y. Xie, C.A. Farrenburg, C.Y. Chin, S. Mun, N.-H.L. Wang, AIChE J. 49 (2003) 2850.
[41] Y. Xie, S.Y. Mun, N.-H.L. Wang, Ind. Eng. Chem. Res. 42 (2003) 1414.
[42] H.J. Lee, Y. Xie, Y.M. Koo, N.H.L. Wang, Biotechnol. Prog. 20 (2004) 179.
[43] Y. Xie, C.Y. Chin, D.S.C. Phelps, C.H. Lee, K.B. Lee, S. Mun, N.-H.L. Wang, Ind. Eng. Chem. Res. 44 (2005) 9904.
[44] K.B. Lee, C.Y. Chin, Y. Xie, G.B. Cox, N.H.L. Wang, Ind. Eng. Chem. Res. 44 (2005) 3249.
[45] S. Mun, Y. Xie, N.-H.L. Wang, Ind. Eng. Chem. Res. 44 (2005) 3268.
[46] K.B. Lee, S. Mun, F. Cauley, G.B. Cox, N.H.L. Wang, Ind. Eng. Chem. Res. 45 (2006) 739.
[47] S.Y. Mun, N.-H.L. Wang, Y.M. Koo, S.C. Yi, Ind. Eng. Chem. Res. 45 (2006) 7241.
[48] S. Mun, N.-H.L. Wang, Ind. Eng. Chem. Res. 45 (2006) 1454.
[49] R. Aris, Ind. Eng. Chem. Fundam. 22 (1983) 150.
[50] L. Riekert, AIChE J. 31 (1985) 863.
[51] D.D. Do, R.G. Rice, Chem. Eng. Sci. 42 (1987) 2269.
[52] F.D. Antia, C. Horváth, J. Chromatogr. 484 (1989) 1.
[53] F.D. Antia, C. Horváth, J. Chromatogr. 550 (1991) 411.
[54] L.R. Snyder, J.W. Dolan, J.R. Gant, J. Chromatogr. 165 (1979) 3.
[55] M.A. Quarry, R.L. Grob, L.R. Snyder, J. Chromatogr. 285 (1984) 1.
[56] M.A. Quarry, R.L. Grob, L.R. Snyder, J. Chromatogr. 285 (1984) 19.
[57] M.A. Quarry, R.L. Grob, L.R. Snyder, Anal. Chem. 58 (1986) 907.
[58] L.R. Snyder, J.W. Dolan, Chem. Anal. (Warsaw, Pol.) 43 (1998) 495.
[59] P.C. Wankat, Rate-Controlled Separations, Elsevier Applied Science, New York, NY, 1990.
[60] R.H. Perry, Perry's Chemical Engineer's Handbook, McGraw-Hill, New York, 1984.
[61] P. Moslemi, A.R. Najafabadi, H. Tajerzadeh, J. Pharm. Biomed. Anal. 33 (2003) 45.
[62] S.F. Chung, C.Y. Wen, AIChE J. 14 (1968) 857.
[63] J.M. Creeth, Biochem. J. 53 (1953) 41.
[64] A.J. Easteal, L.A. Woolf, J. Phys. Chem. 89 (1985) 1066.
[65] E.J. Wilson, C. Geankoplis, Ind. Eng. Chem. Fundam. 5 (1966) 9.
[66] H.S. Fogler, Elements of Chemical Reaction Engineering, Third ed., Prentice-Hall, Inc., Upper Saddle River, New Jersey, 1999.
[67] L.R. Snyder, J.J. Kirkland, J.L. Glajch, Practical HPLC Method Development, John Wiley & Sons, Inc., New York, NY, 1997.
[68] X. Jin, Z. Ma, J. Talbot, N.-H.L. Wang, Langmuir 15 (1999) 3321.